Dalton Transactions

ROYAL SOCIETY OF CHEMISTRY

PAPER

View Article Online
View Journal | View Issue

Cite this: *Dalton Trans.*, 2026, **55**, 6128

Broadband microwave absorption in MoS_2–Co nanocomposites by the synergy of dielectric and magnetic losses

Burak Kıvrak, [a] Hasan Akyıldız, *[a] Oğuzhan Akgöl, [b] Muharrem Karaaslan [b] and Mustafa Akyol [c]

The development of light weight materials with high microwave absorption efficiency is critical for advanced stealth and electromagnetic interference applications. Hybrid composites that integrate dielectric and magnetic components offer enhanced attenuation by leveraging multiple loss mechanisms. To explore this potential, we decorated MoS_2 particles with magnetic Co nanoparticles (Co content ranging from 5 to 20 wt%) and systematically investigated their microwave absorption properties over the 2–18 GHz frequency range. The individual materials and hybrid structures were synthesized using a multi-step strategy involving solution-based methods such as hydrothermal synthesis, chemical reduction of reactants, and sonication. Structural, morphological, compositional, and magnetic analyses collectively confirmed the successful incorporation and uniform dispersion of Co within the nanosheets of the MoS_2 host. Meanwhile, the microwave absorption properties revealed a strong dependence on Co content. Notably, the nanocomposite containing 15 wt% Co exhibited superior performance, achieving a minimum reflection loss of −17.17 dB at 13.84 GHz and an ultra-broad effective absorption bandwidth of 7.51 GHz. This performance is attributed to the synergy between the dielectric, magnetic, and morphologically derived mechanisms. Furthermore, the hybrid design enables tunable interactions with incident waves, facilitating broad frequency coverage and enhanced attenuation. Overall, this work demonstrates the effectiveness of MoS_2–Co nanocomposites and their compatibility with advanced stealth and microwave absorption applications in this frequency range.

Received 2nd February 2026,
Accepted 16th March 2026

DOI: 10.1039/d6dt00271d

rsc.li/dalton

1. Introduction

As the demand for advanced stealth technology grows and concerns over electromagnetic radiation pollution increase, the need for high-performance and light weight microwave absorber materials (MAMs) becomes critical. Electronic devices, such as cell phones and wireless routers, continuously emit electromagnetic radiation across a wide range of frequencies. Although invisible to the human eye, this radiation permeates daily life, potentially affecting human health and the performance of electronic devices.[1,2] In contrast, military applications highlight another dimension of radiation challenges. For example, radar systems rely on microwave frequencies to detect objects, while stealth technologies aim to minimize the reflection of these signals from certain vehicles to evade detection. In modern warfare, electromagnetic stealth has become a key element of defense strategies. Advanced military platforms such as fighter jets, drones, and armored vehicles are specifically engineered to reduce their radar cross-section (RCS), thereby enhancing survivability and mission effectiveness. To achieve this, two primary approaches are employed to reduce RCS: one focuses on structural design modifications, such as angled surfaces and radar-deflecting geometries, while the other involves the use of MAMs.[3] Although structural design strategies provide effectiveness to some extent, they are limited and often insufficient on their own. Consequently, the integration of MAMs is essential to achieve comprehensive stealth capabilities. Specifically, these materials are designed to absorb incident electromagnetic waves (EMWs), converting their energy into thermal or other dissipative forms through various mechanisms. Their effectiveness depends on the presence of efficient dielectric and magnetic components and achieving optimal impedance matching conditions, making material design a fundamental aspect of next-generation stealth technologies.

Among dielectric materials, molybdenum disulfide (MoS_2), a member of the transition metal dichalcogenide family, has

[a]Department of Metallurgical and Materials Engineering, Konya Technical University, 42250 Konya, Türkiye. E-mail: hakyildiz@ktun.edu.tr
[b]Department of Electrical and Electronics Engineering, İskenderun Technical University, Hatay, 31200, Türkiye
[c]Department of Materials Science and Engineering, Adana Alparslan Türkeş Science and Technology University, 01250 Adana, Türkiye

attracted considerable attention due to its layered structure, tunable specific surface area, and favorable electrical properties.[4,5] These features make MoS_2 highly suitable for microwave absorption applications. For example, Ning *et al.* synthesized MoS_2 nanosheets using a top-down exfoliation method and demonstrated its potential as a microwave absorber, achieving a minimum reflection loss (RL_{min}) of −38.42 dB and an effective absorption bandwidth (EAB) of 4.1 GHz at a thickness of 2.4 mm.[6] Similarly, Liang *et al.* employed hydrothermal method to synthesize two-dimensional (2D) MoS_2 nanosheets, achieving an RL_{min} of −47.8 dB at 12.8 GHz with a thickness of 2.2 mm.[7]

Despite the promising potential revealed by single-component systems, the current research field still requires further improvement in microwave absorption performance. To address this, researchers have developed composite structures by integrating dielectric matrices with magnetic nanoparticles (NPs) to enhance microwave absorption efficiency.[8] Specifically, magnetic materials including Fe, Ni, Co, and their oxides (*e.g.*, Fe_3O_4, $CoFe_2O_4$, $NiFe_2O_4$, $NiCo_2O_4$, and Co_3O_4) have been extensively employed in microwave absorption applications.[9–15] These materials contribute to microwave attenuation through various magnetic loss mechanisms, including natural and exchange resonances, as well as eddy current losses in the GHz frequency range. Nevertheless, when magnetic materials are used individually, they also often suffer from poor impedance matching, which significantly limits their overall absorption efficiency.[16] Therefore, a composite approach that harnesses both dielectric and magnetic loss mechanisms to improve the performance of MAMs is widely adopted.

In this context, the present study reports a facile sonication-assisted fabrication of MoS_2–Co nanocomposites designed to achieve enhanced microwave absorption through dielectric–magnetic synergy. Unlike many previously reported systems requiring complex synthesis routes, the proposed approach enables a simple and controllable integration of Co nanoparticles into the MoS_2 matrix. Furthermore, the effect of Co loading (5–20 wt%) on the microwave absorption performance was systematically investigated. The microwave absorption properties of the resulting nanocomposites were evaluated in the 2–18 GHz frequency range using the coaxial waveguide method. Among the samples, the one containing 15 wt% Co exhibited the best performance, achieving an RL_{min} of −17.17 dB at 13.84 GHz and an EAB of 7.51 GHz. These results demonstrate the potential of the optimized MoS_2–Co nanocomposite as a light weight and broadband microwave absorbing material.

2. Experimental process

2.1. Materials

To synthesize MoS_2, Co and MoS_2–Co samples, sodium molybdate dihydrate ($Na_2MoO_4{\cdot}2H_2O$, Sigma-Aldrich, ≥99.0%), thiourea (CH_4N_2S, Alfa Aesar, 99.0%), oxalic acid ($C_2H_2O_4{\cdot}2H_2O$, ≥99.0%), cobalt(II) chloride hexahydrate ($CoCl_2{\cdot}6H_2O$, Sigma-Aldrich, ≥99.0%), and sodium borohydride ($NaBH_4$, Sigma-Aldrich) were utilized as primary reagents. Deionized (DI) water and ethyl alcohol (EA, Tekkim, 96.0%) served as solvents and cleaning agents throughout the synthesis and purification processes.

2.2. Synthesis of flower-like MoS_2

Flower-like MoS_2 particles were achieved through a one-step hydrothermal method based on our previous work.[17] The synthesis procedure is illustrated in Fig. 1a. Initially, 0.1 M $Na_2MoO_4{\cdot}2H_2O$ was dissolved in 110 mL of water and stirred for 10 min, followed by the addition of 41.25 mmol of CH_4N_2S and stirring for an additional 10 min. Subsequently, 8.25 mmol of $C_2H_2O_4{\cdot}2H_2O$ was added, and the mixture was stirred for 60 min. The resulting solution was subjected to hydrothermal treatment at 200 °C for 12 h. The precipitated particles were separated by centrifugation, washed with DI water and EA to ensure purity, and dried at 80 °C for 8 h in an oven.

2.3. Synthesis of Co nanoparticles

The synthesis of Co NPs was carried out through a two-stage process including the chemical reduction of reactants (CRRs) followed by an additional crystallization heat treatment, as illustrated in Fig. 1b. Initially, 1.0 g of $CoCl_2{\cdot}6H_2O$ was dissolved in 25 mL of DI water and stirred at 1200 rpm for 15 min at room temperature (RT) using a magnetic stirrer (Solution A). Separately, 0.5 g of $NaBH_4$ was dissolved in 25 mL of DI water and stirred for 10 min at RT (Solution B). After complete dissolution of both solutions, Solution B was transferred to a dropping funnel and added dropwise (1 drop per second) into Solution A under continuous stirring at 1200 rpm at RT. Upon reaching a critical $NaBH_4$ concentration, gas bubbles appeared, indicating the formation of hydrogen (H_2) gas as a byproduct alongside the reduction of Co ions and the nucleation of nanoparticles. The formation of Co NPs *via* the CRRs method is described by reaction (1), which outlines the reduction of $CoCl_2{\cdot}6H_2O$ by $NaBH_4$ and the accompanying H_2 gas formation.[18] This H_2 gas creates a protective layer at the solution–atmosphere interface, preventing oxidation of Co NPs.[19]

$$2Co_2^{2+} + BH_4^- + 2H_2O \rightarrow 2Co + 2H_2 + 4H^+ + BO_2^- \quad (1)$$

As the reaction progressed, black precipitates formed at the beaker's base, with gas evolution gradually decreasing and ceasing after 4 min, indicating reaction completion. The resulting precipitates (black in color) were centrifuged at 6000 rpm for 10 min and washed sequentially with DI water and EA to remove residual chemicals. Subsequently, the washed products were dried at 60 °C for 6 h under a reduced pressure of 1×10^{-3} mbar.

The crystallization heat treatment was conducted in a tube furnace at 400 °C for 1 h under an Ar/H_2 atmosphere (4 vol% H_2) at 1.1 bar to ensure a reducing environment to prevent the oxidation of Co NPs. Once the furnace reached the designated

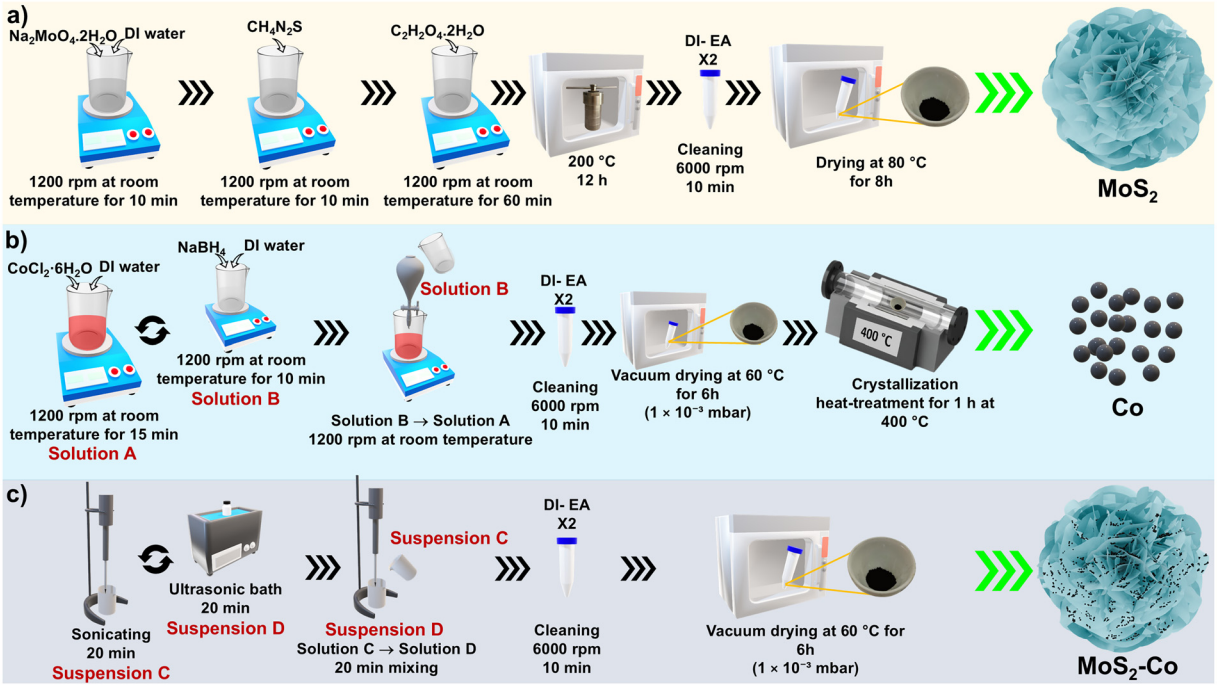

Fig. 1 Schematic illustration of the synthesis procedures for (a) flower-like MoS_2 particles, (b) Co NPs, and (c) MoS_2–Co nanocomposites.

annealing temperature, the Co NPs were transferred to the hot zone for 1 h of annealing. After this period, the samples were retracted to the cold zone of the furnace while maintaining the same atmosphere and allowed to cool to RT.

2.4. Combination of flower-like MoS_2 and Co nanoparticles

To achieve the final composites, Co NPs were combined with MoS_2 particles using a facile sonication method.[17] The procedure is illustrated in Fig. 1c. The nanocomposites were prepared in four distinct weight ratios, ranging from 5 wt% to 20 wt% Co in 5 wt% increments, and were labelled MC1, MC2, MC3 and MC4, respectively, as shown in Table 1.

For instance, the preparation of the MC1 composite, with a total mass of 5 g, began by dispersing 0.25 g of Co NPs in 20 mL of ethanol (Suspension C). This suspension was placed in an ice bath, as illustrated in Fig. 1c, and subjected to sonication for 20 min to ensure a uniform particle distribution. Meanwhile, 4.75 g of MoS_2 was precisely weighed, transferred into a beaker, and dispersed in 20 mL of ethanol using an ultrasonic bath (Suspension D). To enhance particle dispersion throughout the process, both the sonicator and ultrasonic bath were operated simultaneously, as indicated by the dual circular arrows in Fig. 1c. After 20 min of sonication, the Co and MoS_2 suspensions were interchanged between the sonicator and ultrasonic bath and processed for an additional 20 min. Subsequently, Suspension C (Co NPs) was poured into Suspension D (MoS_2) under continuous sonication and mixed for an additional 20 min. Following this step, the resulting suspension was centrifuged at 6000 rpm for 10 min, and the obtained precipitate was dried under vacuum (1×10^{-3} mbar) at 60 °C for 6 h.

Table 1 The content and compositional distribution of the manufactured samples

Sample code	MoS_2 (wt%)	Co (wt%)
MoS_2	100	—
Co	—	100
MC1	95	5
MC2	90	10
MC3	85	15
MC4	80	20

2.5. Characterization techniques

The structural characteristics of the samples were investigated through X-ray diffraction (XRD) with Cu-K_α radiation provided by a Rigaku MiniFlex600 (Cu-K_α = 0.154 nm, 2θ = 10–80°, scan rate of 2° min^{-1}) and Fourier-transform infrared spectroscopy (FT-IR, Jasco FT/IR-6700, 380–4000 cm^{-1}). The morphological features of the samples were examined by scanning electron microscopy (SEM, FEI-Quanta 650D FEG, 5–400kX magnification). The chemical states of elements in the samples were specified using X-ray photoelectron spectroscopy (XPS, Specs Flex-Mod System). Photoelectrons were excited with an Al anode (Kα = 1468.6 eV) in pass energy (PE) mode, with PE = 50 eV. The position of the XPS peaks of the corresponding element is referred to the C 1s peak of carbon, whose energy is taken equal to 286.83 eV. Magnetic properties were determined with a vibrating sample magnetometer (VSM, Quantum Design DynaCool). The microwave characteristics, spanning the S-, C-,

X-, and Ku-bands (2–18 GHz), were measured using a vector network analyzer (VNA, Agilent E8363B PNA). Measurement specimens were prepared by dispersing 30 wt% of pristine MoS_2 particles, pure Co NPs, or MoS_2–Co nanocomposites into an epoxy resin matrix, using a mechanical stirrer at 600 rpm for 30 min to achieve a uniform dispersion of the fillers. The resulting homogeneous mixture was poured into a toroidal mold (outer diameter: 7 mm, inner diameter: 3 mm) and cured at RT for 24 h. Key parameters, including permittivity and permeability, were measured directly, enabling the calculation of performance metrics such as input impedance (Z_{in}), reflection loss (RL), impedance matching, eddy current loss, and attenuation constant. These metrics were derived using eqn (1)–(5):[17]

$$Z_{in} = Z_0\left(\sqrt{\mu_r/\varepsilon_r}\right)\tanh\left[j\left(\frac{2\pi fd}{c}\right)\left(\sqrt{\mu_r\varepsilon_r}\right)\right] \quad (1)$$

$$RL = 20\ \lg\left(\frac{Z_{in}-Z_0}{Z_{in}+Z_0}\right) \quad (2)$$

$$Z = |Z_{in}/Z_0| \quad (3)$$

$$C_0 = \mu''(\mu')^{-2}f^{-1} \quad (4)$$

$$\alpha = \frac{\sqrt{2}\pi f}{c}\times\sqrt{(\mu''\varepsilon''-\mu'\varepsilon')+\sqrt{(\mu''\varepsilon''-\mu'\varepsilon')^2+(\mu'\varepsilon''+\mu''\varepsilon')^2}} \quad (5)$$

In the above equations, ε_r and μ_r represent the complex permittivity ($\varepsilon_r = \varepsilon' - j\varepsilon''$) and permeability ($\mu_r = \mu' - j\mu''$) values, respectively, which define the electromagnetic characteristics of the composite. Here, ε' and μ' denote the real components of permittivity and permeability, while ε'' and μ'' correspond to their imaginary components. Moreover, Z_{in} is the input impedance of the absorber, Z_0 is the impedance of the free space, c is the speed of EMWs in free space, f is the frequency, and d is the layer thickness changing from 1 to 5 mm. Furthermore, eqn (4) quantifies the eddy current loss (C_0), while eqn (5) defines the attenuation constant (α), both of which contribute to the overall absorption performance.

3. Results and discussion

3.1. Structural characteristics

Fig. 2a and b display the XRD patterns of the individual components and the nanocomposite samples, respectively. The vertical purple, turquoise, green, and pink lines appearing at the bottom of these graphs correspond to the diffraction positions of MoS_2, face-centered cubic Co (*fcc*-Co), hexagonal close-packed Co (*hcp*-Co) and B_2O_3, respectively. Analysis of the diffraction pattern of the Co sample, in comparison with the

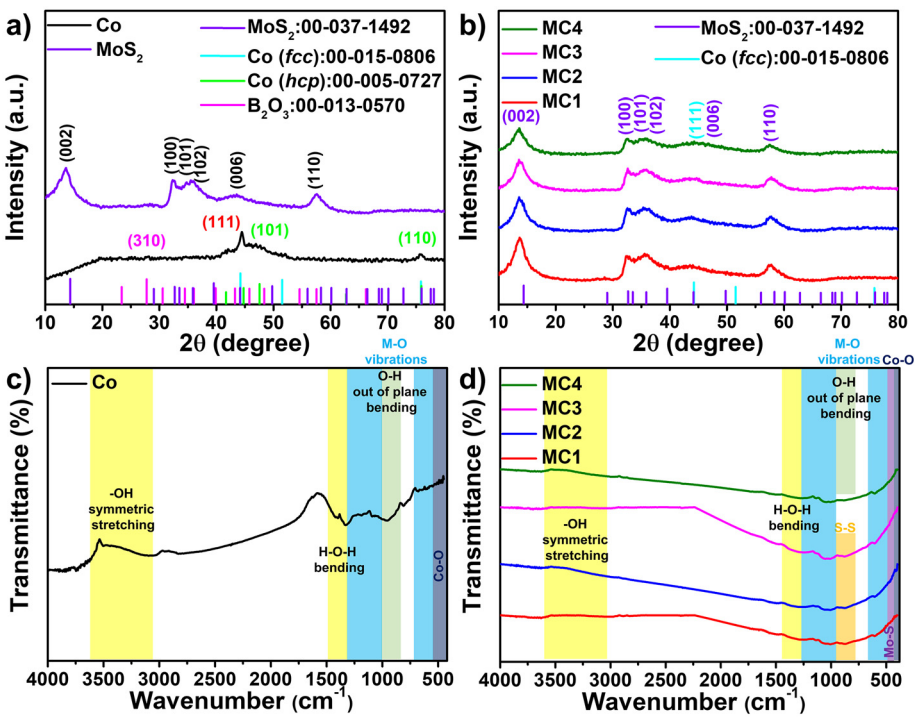

Fig. 2 Structural characteristics of the synthesized samples: XRD patterns of (a) MoS_2 and Co NPs and (b) MoS_2–Co nanocomposites, and FT-IR spectra of (c) Co NPs and (d) MoS_2–Co nanocomposites. The vertical lines given at the bottom of (a) and (b) show the theoretical diffraction positions of MoS_2, Co (*fcc*), Co (*hcp*) and B_2O_3 according to JCPDS card numbers 00-037-1492, 00-015-0806, 00-005-0727, and 00-013-0570, respectively. The characteristic bands in (c) and (d) are highlighted with different colors as a guide to the eye.

reference data, reveals that the Co NPs crystallized in both *fcc* and *hcp* structures, with the most intense peaks observed at 2θ = 44.4° and 48.8°, respectively. According to the literature, *hcp*-Co is the stable phase at RT, whereas *fcc*-Co usually forms during heat treatment under H_2 atmosphere.[20–23] In addition, some studies have reported that *fcc*-Co can also form in the presence of polar molecules, such as water, during synthesis.[24–26] In this study, the Co NPs were synthesized in an aqueous medium and heat-treated under an Ar/H_2 atmosphere; therefore, the coexistence of both *fcc* and *hcp* phases can reasonably be attributed to these experimental conditions. Additionally, a very weak peak at approximately 2θ = 27.86° corresponds to B_2O_3, likely arising from incomplete removal of the BO_2^- byproduct (as indicated in reaction (1)), which could have partially transformed into B_2O_3, leaving trace amounts of boron in the final product. On the other hand, the diffraction pattern of MoS_2 shows no impurity peaks or secondary phases (see Fig. 2a). A slight shift of the (002) peak from its standard position suggests a structural modification in MoS_2, possibly due to increased interlayer spacing. These findings are consistent with our previous study on MoS_2 synthesis, where defect formation and related structural effects were discussed in detail.[17] The diffraction patterns of the MoS_2–Co nanocomposites are shown in Fig. 2b. No significant increase in the intensity of the primary Co peaks was observed as the Co content increased, which can be attributed to the relatively low diffraction intensity of Co compared to MoS_2 and the small weight fraction of Co NPs in the composites. Nevertheless, the (111) peak of Co became slightly more distinct in the patterns of MC3 (15 wt%) and MC4 (20 wt%) with increasing Co loading.

The FT-IR spectra of the Co NPs and MoS_2–Co nanocomposites are presented in Fig. 2c and d, respectively. In each spectrum, the peaks at 3208, 1639, 1400, and 901 cm^{-1} correspond to the symmetric stretching of –OH groups, H–O–H bending, and out-of-plane O–H bending vibrations originating from adsorbed water molecules.[27,28] In the FT-IR spectrum of Co, bands at 553 and 671 cm^{-1} are attributed to the metal–oxygen (M–O) and oxygen–metal–oxygen (O–M–O) stretching vibrations, respectively. Additionally, in the FT-IR spectra of the MoS_2–Co nanocomposites, the peak at 915 cm^{-1} corresponds to S–S vibrations, and the peak at 475 cm^{-1} corresponds to the Mo–S vibrational modes.[29] These results demonstrate that the characteristic peaks of both MoS_2 and Co are present in the FT-IR spectra of the MoS_2–Co nanocomposites, confirming the successful integration of these two components.

3.2. Morphological characteristics

The morphological features of MoS_2 particles and Co NPs are illustrated in Fig. 3. As shown in Fig. 3a, MoS_2 reveals a characteristic three-dimensional (3D) flower-like morphology. The average dimension of the spaces between the nanosheets was calculated as 129.3 nm based on the SEM data and 100 measurements using ImageJ software (Fig. 3b). On the other hand, the as-synthesized Co NPs exhibited a wide size distribution ranging from 15 to 60 nm, with an average particle size (A.P.S.) of 34.11 nm (Fig. 3c–d). These findings indicate that the morphology of MoS_2 and the size of the Co NPs are suitable for the allocation of Co NPs within the spaces of the MoS_2 nanosheets. Furthermore, the Co NPs display a distorted spherical shape, which is likely due to agglomeration (Fig. 3c). After crystallization heat treatment, the particle morphology remains almost unchanged (Fig. 3e), with only a slight increase in A.P.S. to 39.87 nm (Fig. 3f), which indicates modest grain growth during the heat treatment.

Fig. 4 illustrates the SEM images of MoS_2–Co nanocomposites with Co NPs integrated into the MoS_2 host at different loading ratios (5 wt% Co for MC1, 10 wt% Co for MC2, 15 wt% Co for MC3, and 20 wt% Co for MC4). As observed in the low-magnification images (Fig. 4a, d, g and j), the MoS_2 particles retain the spherical-like morphology even after the combination process, indicating that the structural integrity is well preserved. Moreover, the higher-magnification images (Fig. 4b, e, h and k) reveal relatively smooth surfaces, which are likely attributed to the combination process and the stacking of Co NPs between the MoS_2 nanosheets during the synthesis. In addition, the high-magnification SEM images of MC1, MC2, MC3, and MC4 composites (Fig. 4c, f, i and l) further demonstrate that the Co NPs are randomly distributed both on the surfaces and within the interlayer spaces of the nanosheets. The regions marked with yellow circles highlight certain agglomerated areas, where Co NPs appear to have coalesced due to magnetic interactions. Overall, these morphological observations confirm the successful integration of both components, resulting in a well-defined composite architecture. The intercalation of Co NPs within the MoS_2 nanosheet gaps is expected to enhance interfacial polarization and multiple scattering of electromagnetic waves, which may contribute positively to microwave attenuation.

3.3. Composition and chemical state characteristics

The XPS analysis was conducted on the sample with a Co content of 10 wt% (MC2), which served as a reference for the other samples. The corresponding spectra are presented in Fig. 5. As shown in Fig. 5a, the survey spectrum of MC2 confirms the coexistence of Co, Mo, S, C, and O elements, thereby demonstrating the multicomponent nature of the material. The deconvoluted Co 2p spectrum (Fig. 5b) exhibits spin–orbit split peaks at approximately 796 eV (Co $2p_{1/2}$) and 780 eV (Co $2p_{3/2}$), accompanied by two satellite peaks at 801.8 and 785.8 eV. These features indicate partial oxidation of Co, which may result from surface oxidation or exposure to the synthesis environment.[30] Similarly, deconvolution of the Mo 3d spectrum (Fig. 5c) reveals four distinct peaks, two of which are assigned to the Mo^{4+} $3d_{3/2}$ and $3d_{1/2}$ levels of the 1T phase, along with a minor S 2s contribution at ~225 eV.[31] In addition, small shoulders near 233.0 and 235 eV, attributed to Mo^{6+}, suggest the presence of oxidized molybdenum species such as MoO_3 or MoO_x on the surface.[32] The S 2p spectrum (Fig. 5d) displays the characteristic S^{2-} peaks at ~161 eV (S $2p_{3/2}$) and ~163 eV (S $2p_{1/2}$), typical of MoS_2. However, a noticeable S^{6+} peak at ~168 eV indicates the existence of sulfate-like species

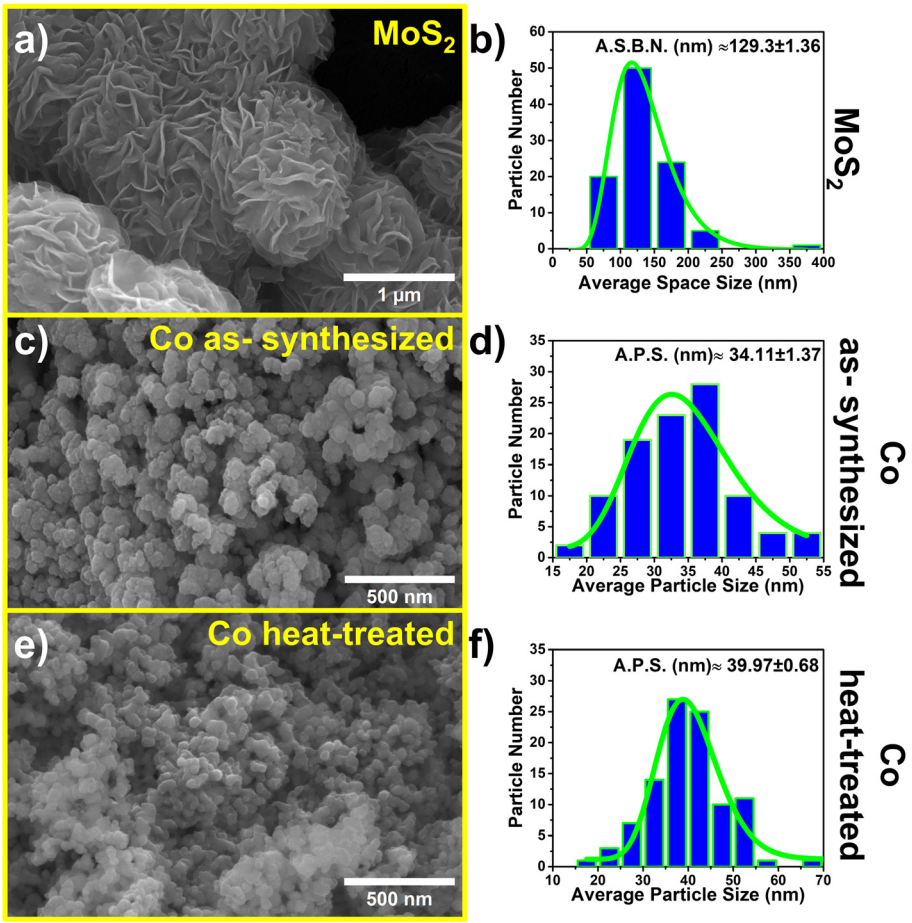

Fig. 3 Morphological characteristics of (a and b) MoS_2, (c and d) as-synthesized Co and (e and f) heat-treated Co NPs (the A.S.B.N. and A.P.S abbreviations refer to "average space between nanosheets" and "average particle size," respectively).

(SO_x) on the surface, likely arising from oxidation processes.[33] Due to the pronounced intensity of this sulfate peak, deconvolution of the S^{2-} doublet could not be performed accurately. Meanwhile, the O 1s spectrum (Fig. 5e) shows a broad feature centered around 531 eV, which can be deconvoluted into contributions from lattice oxygen (*e.g.*, MoO_x), adsorbed oxygen, and hydroxyl groups. Overall, the presence of satellite peaks, Mo^{6+} species, and sulfate groups in the XPS spectra indicates partial surface oxidation of the composite. This phenomenon is likely related to the sonication-assisted synthesis or subsequent exposure to air during storage. Considering the susceptibility of metal particles to atmospheric oxidation, the sonication process may have exposed sulfur edge sites that facilitate oxygen bonding, rendering Mo atoms more susceptible to oxidation and leading to the observed surface characteristics.

3.4. Magnetic characteristics

The room-temperature magnetization (M–H) curves of the Co NPs and MoS_2–Co nanocomposites are shown in Fig. 6, which compares the hysteresis loops of Co NPs before and after the crystallization heat treatment process. As evident from the figure, both samples exhibit clear ferromagnetic behavior at RT, with distinct saturation magnetization (M_s) values of 13.1 emu g^{-1} for the as-synthesized sample and 90.4 emu g^{-1} for the heat-treated Co NPs. This pronounced enhancement in magnetization after thermal treatment suggests that the process improves the magnetic ordering of Co NPs, likely due to the enhanced crystallinity and/or the reduced structural defects. Fig. 6b displays the hysteresis loops of MoS_2–Co nanocomposites. As expected, the overall magnetization values of the composites are lower than those of pure Co NPs, which can be attributed to the intrinsically weak magnetic nature of the MoS_2 host. Moreover, the figure clearly indicates that increasing the Co content leads to a gradual rise in the magnetization of the composites. The M_s values for the MC1, MC2, MC3, and MC4 samples were determined as 7.6, 10.1, 13.2, and 18.0 emu g^{-1}, respectively. Another notable difference between pure Co NPs and MoS_2–Co nanocomposites lies in their coercive field (H_c) values. While the H_c value of pure Co NPs is 0.0630 T, the MoS_2–Co nanocomposites exhibit lower coercivity values of 0.0237, 0.0220, 0.0216, and 0.0228 T for MC1, MC2, MC3 and MC4, respectively. Since the H_c parameter reflects the ease of magnetic domain reorientation, the

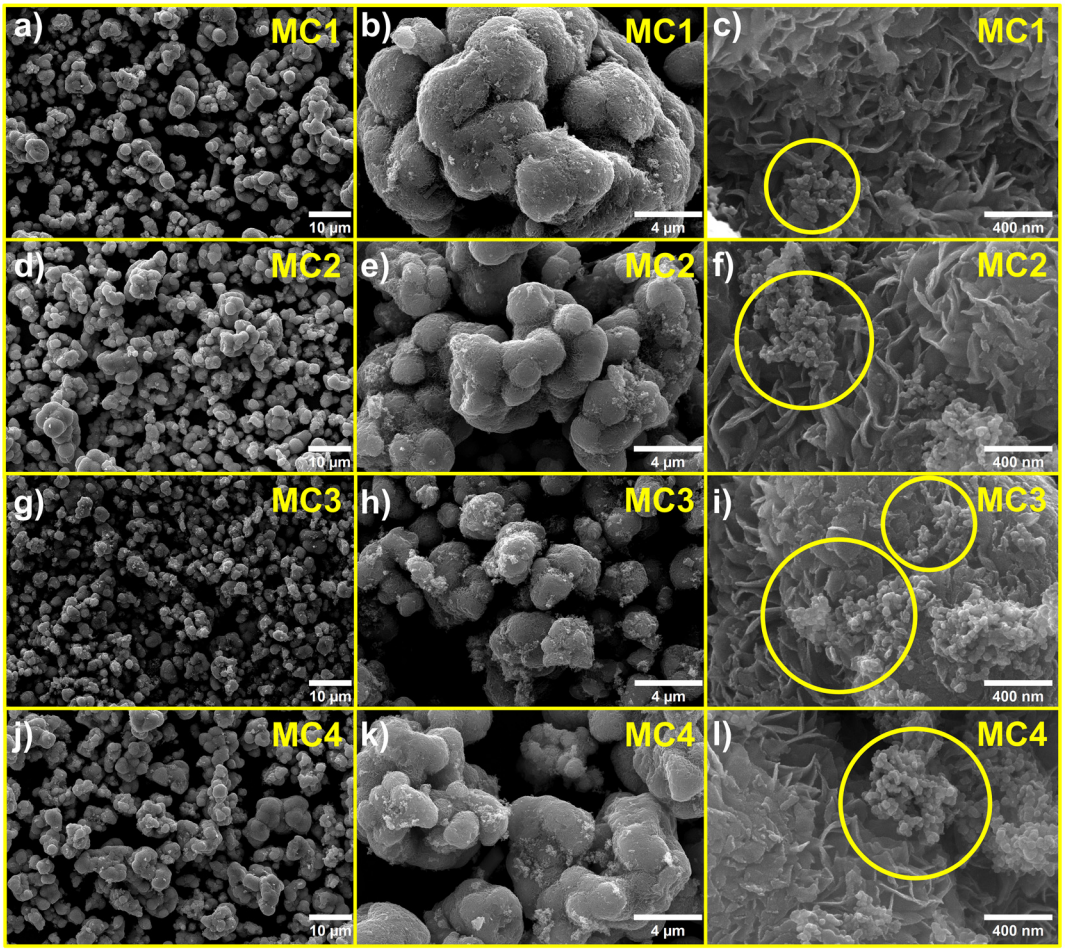

Fig. 4 Morphological characteristics of MoS_2–Co nanocomposites: (a–c) MC1 (5 wt% Co), (d–f) MC2 (10 wt% Co), (g–i) MC3 (15 wt% Co), and (j–l) MC4 (20 wt% Co).

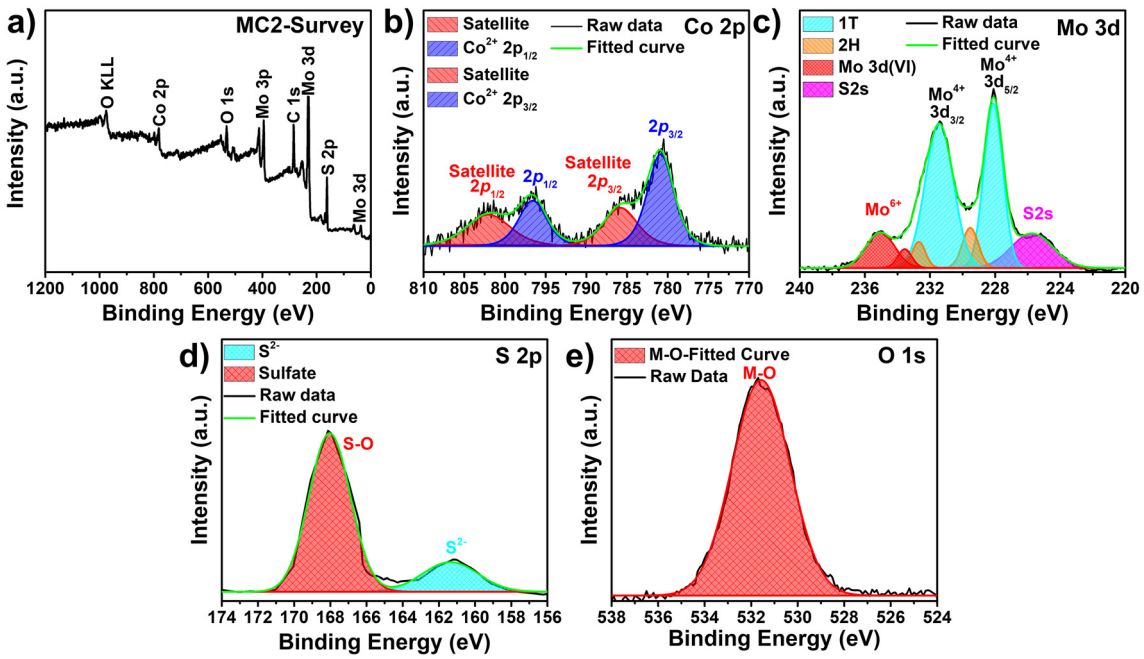

Fig. 5 XPS results of MoS_2–Co (10 wt% Co): (a) survey, (b) Co 2p, (c) Mo 3d, (d) S 2p, and (e) O 1s spectra.

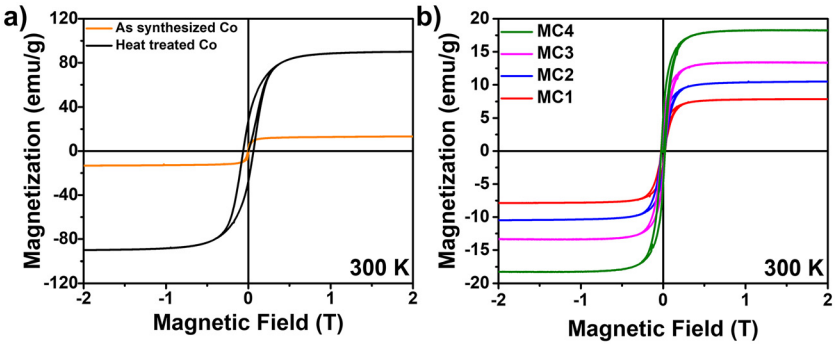

Fig. 6 Room temperature magnetic hysteresis curves of (a) Co NPs before and after crystallization heat treatment and (b) MoS_2–Co nanocomposites.

reduced H_c values of the composites indicate that their magnetic moments can be more easily manipulated under a low external magnetic field. Thus, these results confirm the successful integration of Co and MoS_2 components, yielding tunable magnetic properties that increase proportionally with the Co content.

3.5. Electromagnetic characteristics

3.5.1. Dielectric behavior. To achieve high absorption performance, two main factors must be considered: optimal impedance matching between air and the absorber, and the material's ability to effectively attenuate the penetrated wave energy throughout its relative thickness. These factors are directly related to the electromagnetic parameters of the absorber, as shown in the previous section (see section 2.5). The key electromagnetic parameters, complex permittivity and complex permeability, provide critical insights into the specific absorption behavior of the material. Specifically, the real parts of permittivity (ε') and permeability (μ') represent the material's capacity to store electric and magnetic energy, while the imaginary parts (ε'' and μ'') reflect the material's ability to dissipate energy through various loss mechanisms. Fig. 7 presents the real and imaginary components of permittivity and permeability as a function of frequency for MoS_2–Co nanocomposites, with the values for pure Co NPs also included for comparison. The dielectric and magnetic behavior of pure MoS_2 is not presented here, as it has already been comprehensively analyzed in our previous study.[17] As illustrated in Fig. 7a, ε' values decrease with increasing frequency, indicating a strong dielectric dispersion effect.[34] This frequency-dependent behavior can be attributed to dipolar polarization at the material surfaces, which plays a significant role in microwave absorption.[35–37] Moreover, the bare Co sample has the lowest ε'value (~4.12, the highest value over 2–18 GHz) among all measured samples, reflecting its limited electric energy storage capability. For the MoS_2–Co composites, the ε' values do not show a clear monotonic dependence on Co content. Specifically, the MC1 sample exhibits the highest ε' value (~6.16) at around 2 GHz, indicating superior electric energy storage capacity, while MC2 shows a slightly lower but comparable ε' value (~5.94 at 2 GHz) throughout the 2–18 GHz range. The MC4 sample follows these two with a moderate ε' value (~4.81, the highest value over 2–18 GHz), whereas MC3 exhibits a value (~4.40) close to that of bare Co, suggesting that the dielectric storage ability of the composite does not increase proportionally with Co addition.

Fig. 7b shows the variation of the imaginary part of permittivity (ε'') as a function of frequency for Co NPs and MoS_2–Co nanocomposites. As can be seen from this figure, no distinct trend is observed among the samples, and all ε'' values appear

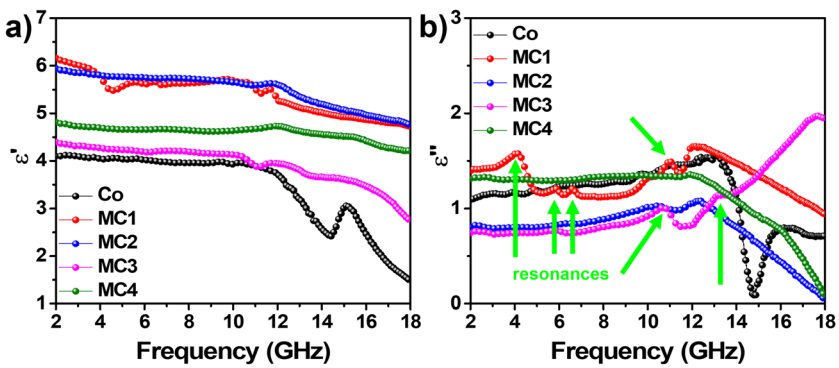

Fig. 7 (a) Real part and (b) imaginary part of permittivity values of Co NPs, MC1, MC2, MC3, and MC4 samples with respect to frequency.

relatively close, accompanied by several resonance peaks. Specifically, the MC3 sample exhibits the highest ε'' value of 1.97 at around 17 GHz, demonstrating superior dielectric loss capability. This sharp increase occurs after approximately 15 GHz, whereas at lower frequencies, the MC3 plot remains the lowest among all samples. Following MC3, the MC1 sample shows an ε'' value of 1.65, while bare Co NPs, MC4, and MC2 show their highest values of 1.57, 1.16, and 1.09, respectively. Additionally, the resonance peaks observed in the ε'' plots at specific frequencies suggest the coexistence of multiple polarization mechanisms within the absorbers. Similar resonance behavior reported in the literature supports that these peaks are associated with dipolar orientation and interfacial polarization mechanisms.[38–40] According to Maxwell–Wagner theory, under an alternating electromagnetic field, charge carriers accumulate at heterogeneous interfaces due to restricted charge mobility across boundaries, leading to interfacial polarization.[40] Thus, the observed resonances and elevated dielectric parameters provide evidence of both dipolar and interfacial polarization mechanisms. It is noteworthy that while higher real and imaginary dielectric values indicate greater energy storage and dissipation capabilities, they may also cause impedance mismatch, potentially reducing overall absorption performance (see eqn (1)–(3)). Additionally, based on free-electron theory ($\varepsilon'' = \sigma/2\pi f\varepsilon_0$), the conductive contribution to ε'' is related to the material's electrical conductivity. Thus, an increase in ε'' typically reflects enhanced electrical conductivity within the absorber.[41]

The real (ε') and imaginary (ε'') components of permittivity, along with the associated dielectric loss mechanisms, can be further analyzed using Cole–Cole plots derived from the following equations.

$$\varepsilon' = \varepsilon_\infty + \frac{\varepsilon_s - \varepsilon_\infty}{1 + (j2\pi f\tau)^2} \quad (6)$$

$$\varepsilon'' = \frac{2\pi f\tau(\varepsilon_s - \varepsilon_\infty)}{1 + (2\pi f\tau)^2} = \frac{\varepsilon_s - \varepsilon_\infty}{1 + \omega^2\tau^2}\omega\tau + \frac{\sigma}{2\pi f\varepsilon_0} = \varepsilon''_p + \varepsilon''_c \quad (7)$$

$$\left(\varepsilon' - \frac{\varepsilon_s + \varepsilon_\infty}{2}\right)^2 + (\varepsilon'')^2 = \left(\frac{\varepsilon_s - \varepsilon_\infty}{2}\right)^2 \quad (8)$$

In the above equations, τ represents the relaxation time, ε_s denotes the static dielectric constant, and ε_∞ signifies the dielectric constant at infinite frequency. As indicated, the imaginary component ε'' consists of two contributions: polarization relaxation loss (ε''_p) and conductive loss (ε''_c).[42,43] Polarization loss (ε''_p) dominates in the medium- and high-frequency regions, arising from charge accumulation at heterointerfaces and interfacial polarization processes. This mechanism is reflected by the multiple semicircular arcs in the Cole–Cole plots. Conduction loss (ε''_c) originates from the directional migration and collision of charge carriers within the conductive network, which converts electromagnetic energy into thermal energy. In Cole–Cole plots, this behavior is often manifested as a linear tail in the low-frequency region.[44,45] Cole–Cole plots typically yield semicircular arcs, each representing a distinct dielectric relaxation process. Furthermore, the presence of multiple semicircles indicates the coexistence of several relaxation mechanisms.[46,47] Fig. 8 presents the Cole–Cole plots of the MoS_2–Co nanocomposites together with that of Co NPs. The green numbers in the plots denote the number of relaxation events and the specific frequencies at which they occur. As seen in Fig. 8a, the Co NPs exhibit multiple distorted semicircles, implying the coexistence of several dielectric relaxation processes, most likely originating from both dipolar and interfacial polarization processes.[48] These effects are attributed to the nanoscale dimensions of the magnetic particles and enhanced interfacial interactions between them.[49] Such interfacial effects promote uneven charge distribution, which strengthens interfacial polarization and contributes positively to microwave absorption performance. Similarly, the Cole–Cole plots of MoS_2–Co nanocomposites (Fig. 8b–e) exhibit multiple semicircles, confirming the presence of multiple loss mechanisms, including defect-induced polarization, dipolar polarization, and interfacial polarization. In addition, the appearance of elongated tails in these plots is indicative of conductive losses within the absorbers, suggesting that conductivity loss plays a significant role in the absorption process.[50] Overall, these Cole–Cole features can be ascribed to structural defects (as confirmed by the XRD and XPS analyses) within MoS_2 that act as charge-trapping centers, inducing local dipolar polarization, as well as to the unique morphological configuration that promotes the formation of heterogeneous interfaces. These heterogeneous interfaces lead to uneven spatial charge accumulation, thereby enhancing interfacial polarization effects.[51] Thus, together with the observed tail-like features associated with conductivity losses, it can be concluded that interfacial, defect-induced, and conductive loss mechanisms collectively contribute to the overall dielectric loss and microwave absorption performance of the MoS_2–Co nanocomposites.

3.5.2. Magnetic behavior. Fig. 9 illustrates the real (μ') and imaginary (μ'') components of complex permeability as a function of frequency for Co NPs, MC1, MC2, MC3, and MC4 samples. Generally, higher μ' values indicate an enhanced ability of the absorber to store magnetic energy, whereas higher μ'' values represent its capacity to dissipate magnetic energy. The variation of μ' values with frequency is shown in Fig. 9a. As illustrated, MC2 and MC4 maintain relatively stable μ' values across the entire frequency range, while the other samples exhibit noticeable fluctuations. The highest μ' value is observed for the MC1 sample (1.30), followed by the Co sample (1.26) over the 2–18 GHz range. Although no clear trend is observed with increasing Co content, the MC3 sample maintains relatively stable and moderately high μ' values in the 5–12 GHz range, implying an enhanced magnetic energy storage capability within this frequency window. Fig. 9b illustrates the behavior of the imaginary component as a function of frequency. Among all samples, MC1 exhibits the highest μ'' value (0.49) and strong resonance behavior (steeper slope of the peaks) at lower frequencies, indicating the presence of strong natural resonance loss, particularly around 4–5 GHz.[52]

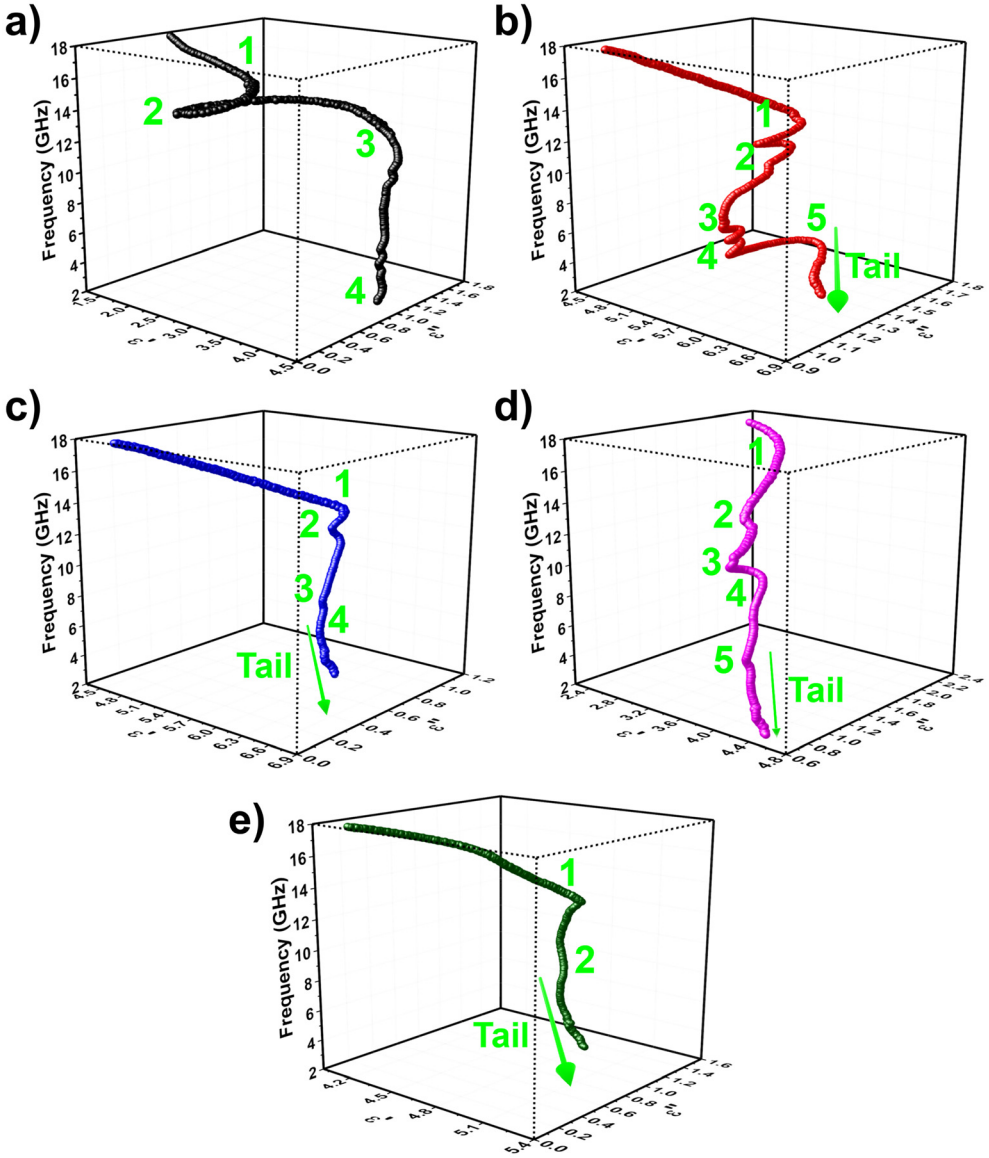

Fig. 8 Cole–Cole plots of (a) Co NPs, (b) MC1, (c) MC2, (d) MC3, and (e) MC4 samples.

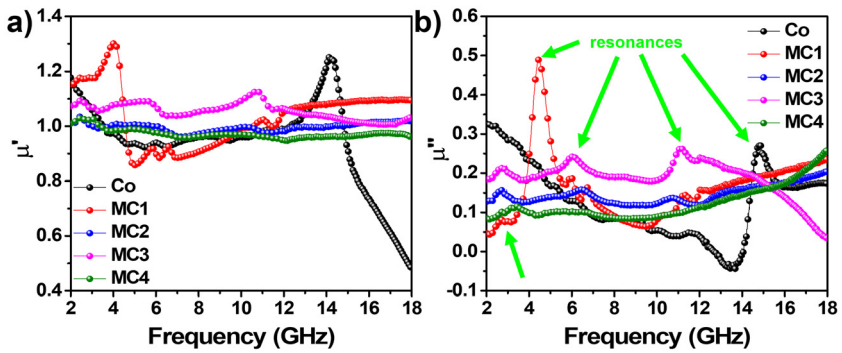

Fig. 9 (a) Real part and (b) imaginary part of permeability values of Co NPs, MC1, MC2, MC3, and MC4 samples with respect to frequency.

Co NPs follow with the second-highest μ'' value (0.27). Meanwhile, MC3 exhibits stable and moderately high μ'' values in the 6–14 GHz range. Consistent with its behavior for the real component, it does not reach the peak values of the MC1 or Co samples. Additionally, around 13 GHz, the μ'' value of Co NPs decreases to negative values, indicating the presence of the eddy currents and radiation of energy from the absorber.[35,46,53] It is well known that the presence of magnetic resonances is typically identified by the appearance of resonance peaks in the μ''–f plot.[54–57] Thus, the observation of multiple resonance peaks in this graph indicates the coexistence of both exchange and natural resonance mechanisms, where exchange resonance generally appears at higher frequencies and natural resonance occurs at lower frequencies.[42,54] Furthermore, natural resonance can be expressed by the ferromagnetic resonance theory:[52]

$$2\pi f_r = rH_a \quad (9)$$

$$H_a = 4|K_1|/3\mu_0 M_s \quad (10)$$

$$|K_1| = \mu_0 M_s H_c/2 \quad (11)$$

where f_r is the natural resonance frequency, r is the gyromagnetic ratio, H_a is the magnetic anisotropy energy, and $|K_1|$ is the anisotropic coefficient. The relationship between H_c and H_a indicates that higher coercivity corresponds to stronger magnetic anisotropy.[52] As shown in Fig. 6, the Co nanoparticles exhibit the highest coercivity value of 0.0630 T, indicating stronger internal magnetic anisotropy, followed by the MC1 sample with 0.0237 T. The enhanced anisotropy can promote magnetic resonance behavior in the GHz region, contributing to magnetic loss mechanisms, which is consistent with the permeability spectra shown in Fig. 9.

Magnetic losses within the GHz range primarily originate from natural resonance, exchange resonance, and eddy current losses.[58] Among these mechanisms, eddy current losses emerge in conductive regions of the material as the magnetic field oscillates. The eddy current loss is calculated using eqn (4), and Fig. 10 illustrates the eddy current loss graphs of the synthesized samples as a function of frequency.[59] When eddy current loss dominates the absorption mechanism, the frequency-dependent C_0 plot typically exhibits a linear trend. Conversely, any fluctuations in the plot indicate contributions from natural and exchange resonance losses.[60] In the case of Co NPs, the C_0 plot exhibits a wavy pattern, confirming the dominance of natural and exchange resonance losses (black plot in Fig. 10). This aligns with the magnetic properties of Co, where these resonance mechanisms are more pronounced than the eddy current effects. Conversely, the MC4 sample shows an almost linear C_0 plot across 8–18 GHz, suggesting that eddy current loss is the primary contributor in this frequency range. Furthermore, the MC1, MC2 and MC3 samples display distinct resonance peaks, particularly beyond 12 GHz, revealing a combination of eddy current and resonance-driven losses. Overall, the magnetic losses in the composites arise from a delicate balance between eddy currents and magnetic

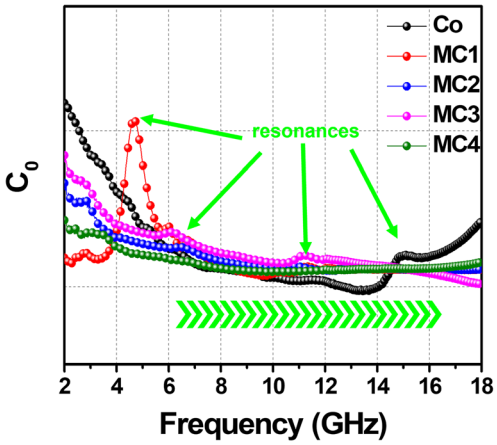

Fig. 10 The variation of eddy current loss for Co NPs, MC1, MC2, MC3, and MC4 samples with respect to frequency.

resonances, with the dominant mechanism varying depending on the composition and frequency range. Therefore, the coexistence of these multiple magnetic loss mechanisms, including natural resonance, exchange resonance, and eddy current loss, is expected to synergistically enhance the microwave attenuation capability of the MoS_2–Co nanocomposites.

3.5.3. Microwave absorption behaviour. As mentioned in section 2.5, the microwave absorption properties of the fabricated samples were evaluated using a VNA across the frequency range of 2–18 GHz. Fig. 11 presents the 3D mapping, 2D contour and 1D RL graphs of the fabricated samples. The black dashed lines in these graphs represent the −10 dB threshold, which corresponds to 90% absorption of the incident EMWs. The microwave absorption properties of pure MoS_2 particles were previously reported.[61] Bare MoS_2 showed promising results, and the best sample exhibited an RL_{min} of −13.05 dB and an EAB of 2.51 GHz at a thickness of 5 mm. Therefore in the current study, the RL behavior of Co NPs was initially evaluated. Fig. 11a–c illustrate the RL graphs of pure Co NPs, revealing that the sample with a thickness of 4 mm (pink plot in Fig. 11c) exhibits an RL_{min} of −14.60 dB and a notably wide EAB of 5.36 GHz (Fig. 11b). Moreover, the 5 mm thick sample (Fig. 11a) demonstrates an exceptionally high RL_{min} of −33.39 dB at 17.91 GHz, corresponding to 99.95% absorption, along with an EAB of 1.89 GHz. These results clearly indicate that Co NPs are more efficient in attenuating EMWs compared to pure MoS_2 particles.

In addition, the impedance matching characteristics, illustrated in Fig. 12a–c, provide complementary evidence for this enhanced performance. As evident from these figures, the $|Z_{in}/Z_0|$ values for Co NPs approach the optimal value of 1, indicating enhanced penetration of the EMWs into the material. Consequently, this favorable impedance matching correlates with the observed RL data, confirming that the superior wave attenuation of bare Co NPs arises from both effective wave penetration and energy dissipation within the absorber, compared to bare MoS_2 particles.

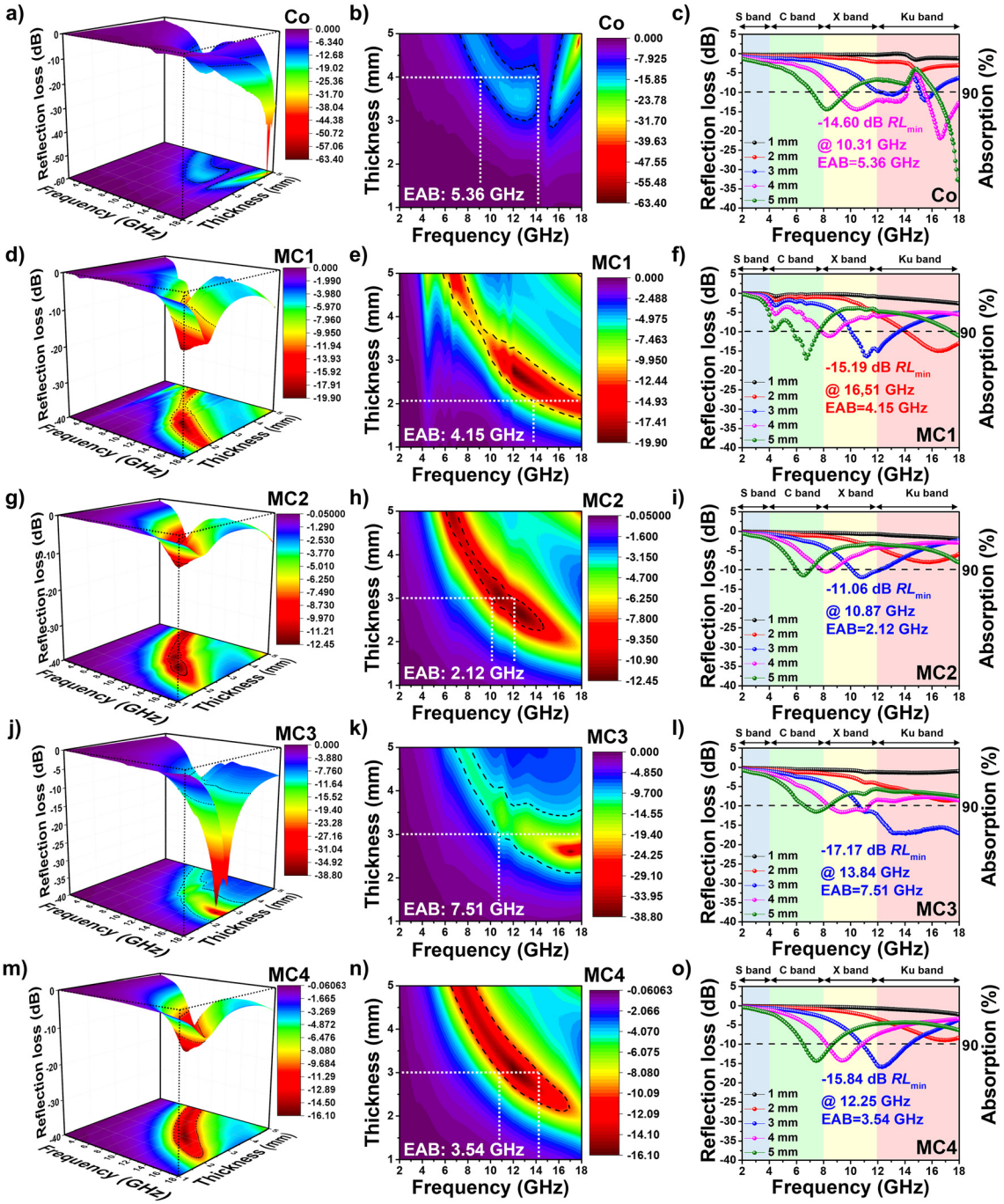

Fig. 11 3D mapping, 2D contour and 1D RL graphs of (a–c) Co NPs, (d–f) MC1, (g–i) MC2, (j–l) MC3, and (m–o) MC4 samples.

Fig. 11d–o present the RL graphs for MoS_2–Co nanocomposites. The corresponding absorption values are summarized in Table 2. As shown in Fig. 11d–f, the introduction of 5 wt% Co into MoS_2 results in only minimal changes in the EAB, although a slight increase in the RL_{min} value is observed. For instance, the MC1 sample, at 2 mm thickness, exhibited an RL_{min} of −15.19 dB at 16.51 GHz with an EAB of 4.15 GHz. However, increasing the Co content to 10 wt% led to a decline in absorption performance. Fig. 11g–i show that the MC2 sample, at 3 mm thickness, achieved an RL_{min} of −11.06 dB at 10.87 GHz with a reduced EAB of 2.12 GHz. The corresponding impedance matching plots (Fig. 12g–i) reveal $|Z_{in}/Z_0|$ values significantly above the optimal threshold of 1, indicating poor EMW penetration and explaining the diminished microwave absorption performance of MC2. In contrast, further increasing the Co content to 15 wt% resulted in a marked improvement in absorption efficiency. The MC3 sample, at 3 mm thickness, exhibited an RL_{min} of −17.17 dB at 13.84 GHz and

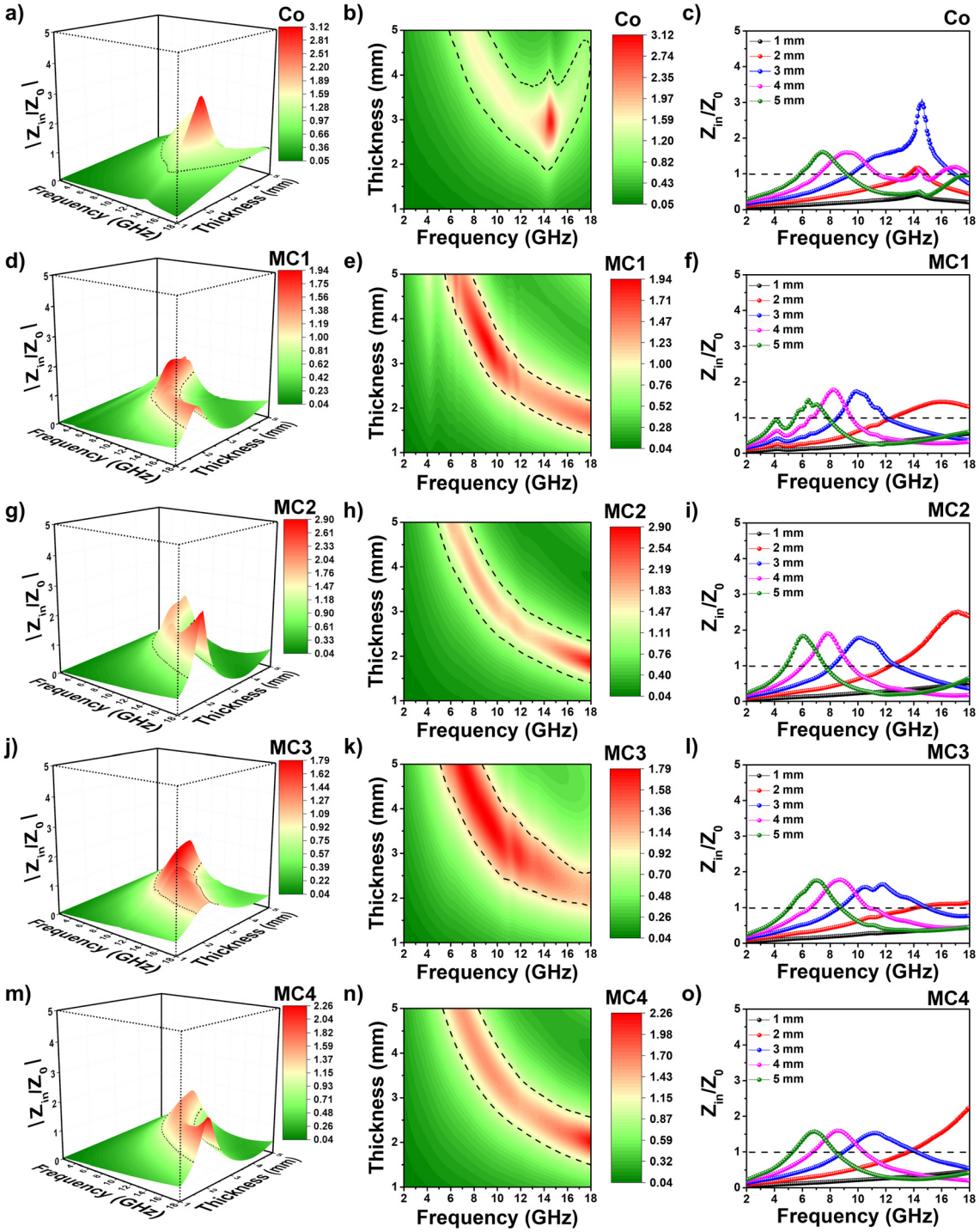

Fig. 12 3D mapping, 2D contour and 1D impedance matching graphs of (a–c) Co NPs, (d–f) MC1, (g–i) MC2, (j–l) MC3, and (m–o) MC4 samples.

an exceptional EAB of 7.51 GHz (Fig. 11j–l). The enhanced microwave absorption performance of MC3 is further supported by its impedance matching characteristics (Fig. 12j–l). The impedance matching variation with Co content could be attributed to both particle agglomeration and percolation effects. At 10 wt% Co, the magnetic filler might be insufficient to form a continuous conductive network, and agglomeration may lead to localized clusters, causing impedance mismatch and higher reflection. When the Co content increases to 15 wt%, the particle volume likely exceeds the percolation threshold, possibly forming a more continuous network. This improved conductivity may enhance interfacial polarization and help balance permittivity and permeability, resulting in better impedance matching and stronger microwave absorp-

Table 2 Microwave absorption performances of the manufactured samples

Sample code	Thickness (mm)	RL_{min} (dB)	Frequency (GHz)	EAB (@−10 dB)
Co	3	−12.27	15.51	1.19
	4	−14.60	10.31	5.36
	5	−33.39	17.91	1.89
MC1	2	−15.19	16.51	4.15
	3	−16.57	11.16	3.65
	5	−17.06	6.73	1.99
MC2	3	−11.06	10.87	2.12
	4	−10.59	8.20	0.97
	5	−11.57	6.50	1.14
MC3	3	−17.17	13.84	7.51
	4	−11.85	9.41	3.17
	5	−11.65	7.43	1.71
MC4	3	−15.84	12.25	3.54
	4	−14.32	9.37	2.86
	5	−14.46	7.42	2.33

tion. Finally, the MC4 sample, containing 20 wt% Co, exhibited an RL_{min} of −15.84 dB at 12.25 GHz and an EAB of 3.54 GHz at 3 mm thickness (Fig. 11m–o). As shown in the impedance matching plots (Fig. 12m–o), the $|Z_{in}/Z_0|$ values are comparable to those of MC3, indicating favorable impedance matching that supports efficient wave penetration. Overall, these results demonstrate that combining MoS_2 with Co significantly enhances the microwave absorption properties, particularly by broadening the EAB. This improvement is critical for the development of advanced MAMs, as it enables efficient EMW absorption over a wider frequency range, which is essential for stealth and other high-performance EMW attenuation applications.

The absorption performance of the samples was further evaluated through the calculation of the attenuation constant (α) using eqn (5), with the results presented in Fig. 13. As indicated by eqn (5), α reflects the combined influence of dielectric permittivity and magnetic permeability on EMW attenuation. As seen in the figure, Co NPs (black plot) maintain a high attenuation constant between 8 and 14 GHz, followed by a gradual decline at higher frequencies. Among the MoS_2–Co

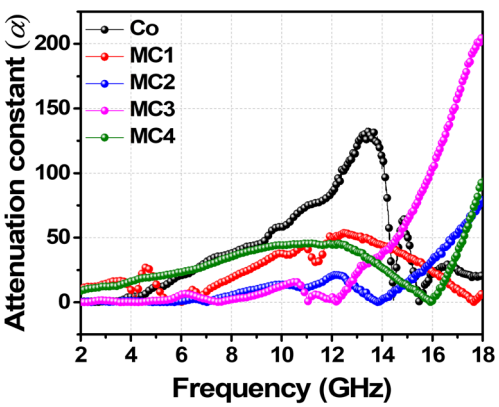

Fig. 13 The variation of attenuation constant for Co NPs, MC1, MC2, MC3, and MC4 samples with respect to frequency.

nanocomposites, the MC3 sample exhibits a notable increase in the attenuation constant beyond 12 GHz, surpassing all other samples in this frequency range. However, as mentioned earlier, an excessively high attenuation constant does not necessarily guarantee optimal performance, since it may lead to impedance mismatch.[16] Therefore, the overall effectiveness of MC3 depends on achieving proper impedance matching in addition to maintaining high α values.

To quantitatively evaluate the impedance matching performance of the samples, the area fraction where $|Z_{in}/Z_0|$ falls within the optimal range of 0.8–1.2 was calculated from the impedance maps, and the results are displayed in Fig. 14. Among all samples, the Co sample exhibits the highest area fraction of 22.53%, indicating superior impedance matching compared to the other samples (MC1: 15.04%, MC2: 12.58%, MC3: 21.10%, and MC4: 15.04%). This trend highlights that controlled Co incorporation can substantially enhance the effective matching area relative to the base material. Focusing on the Co-incorporated composites, MC3 achieves the highest matching performance with an area fraction of 21.09%, demonstrating that an optimal level of Co incorporation maximizes broadband impedance matching. MC1 and MC4 show an intermediate value of 15.04%, while MC2 exhibits the narrowest matching region at 12.58%. This concentration-dependent trend emphasizes that excessive or insufficient Co content can reduce the effective matching region, particularly at the band edges. However, it is important to note that optimal microwave absorption requires not only favorable impedance matching but also sufficient electromagnetic energy dissipation governed by the attenuation constant (α).[62] Therefore, impedance matching determines the ability of incident electromagnetic waves to penetrate the absorber, whereas the α reflects the material's capability to dissipate the absorbed energy. In this context, MC3 presents a well-balanced performance, combining a high matching area fraction (21.10%) with an elevated attenuation constant, as shown in Fig. 13 and 14. This synergistic balance between impedance matching and attenuation capability enables MC3 to effectively convert incident EMWs into thermal energy, highlighting its superiority as an absorber. Therefore, although the Co sample alone achieves the highest impedance matching, MC3 emerges as the most efficient overall absorber due to its optimal combination of impedance matching and attenuation capability. These findings demonstrate that the optimized dielectric–magnetic synergy and balanced impedance matching enable the MC3 nanocomposite to achieve superior broadband microwave absorption performance.

3.5.4. Possible loss mechanisms. The loss tanget plots are valuable for identifying the dominant mechanisms in microwave absorbers. In general, the mechanism corresponding to the higher loss tanget value contributes more significantly to the overall absorption behavior. Fig. 15 illustrates the variation of dielectric (δ_ε) and magnetic (δ_μ) loss tangents with frequency. As seen in these figures, for the Co, MC3 and MC4 samples, the dielectric and magnetic loss tangent values are relatively close. However, the dielectric loss tangent remains

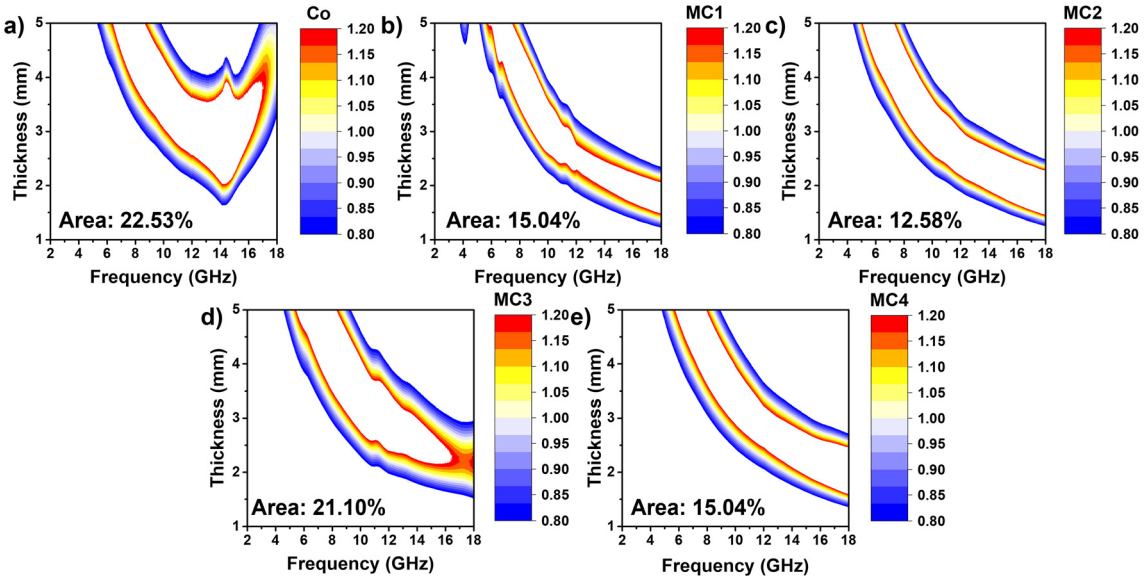

Fig. 14 2D illustration and area fraction of $|Z_{in}/Z_0|$ within the optimal range of 0.8–1.2.

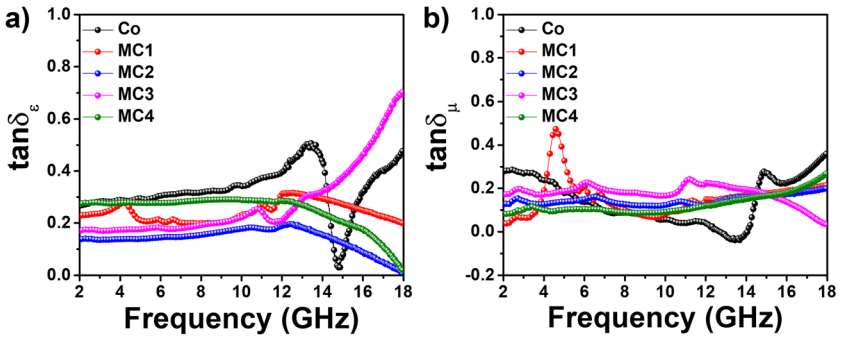

Fig. 15 Loss tanget graphs of Co NPs, MC1, MC2, MC3, and MC4 samples: (a) dielectric loss tanget and (b) magnetic loss tanget.

slightly higher throughout the frequency range. This indicates that while both dielectric and magnetic losses contribute to the attenuation of EMWs, dielectric losses play a slightly more dominant role. On the other hand, for the MC1 and MC2 samples, the magnetic loss tangent exhibits comparatively higher values, indicating that magnetic losses contribute more significantly to their absorption behavior. The enhanced and balanced dielectric and magnetic loss tangents in MC3 correlate strongly with its higher α and broader bandwidth, suggesting that the synergy between these loss processes is key to its superior performance. Therefore, these observations demonstrate that achieving a balanced contribution from both dielectric and magnetic losses is crucial for optimizing microwave absorption performance.

Among all samples, MC3 exhibits the most favorable balance, resulting in enhanced attenuation and a broader EAB. Moreover, for the Co sample, the δ_μ exhibits negative values in the 12.5–14 GHz frequency range. These negative values originate from the imaginary part of permeability (μ'') becoming negative while μ' remains positive (see Fig. 9), a behavior associated with the post-resonance region of the ferromagnetic response.[63] In this regime, the phase lag between the magnetization and the applied electromagnetic field causes μ'' to cross below zero, indicating that the material partially re-radiates the stored magnetic energy rather than dissipating it as heat.[64]

To gain deeper insight into the origins of the excellent microwave absorption performance of the MoS_2–Co nanocomposite, the possible loss mechanisms depicted in Fig. 16 are discussed by correlating structural features with electromagnetic parameters. First, the flower-like morphology of MoS_2, decorated with Co nanoparticles, promotes multiple reflections and scattering of incident EMWs, effectively extending the propagation path and enhancing energy dissipation. This morphological advantage is further supported by the presence of lattice defects in MoS_2, as confirmed by XRD and XPS analyses. These defects induce localized polarization centers, which significantly contribute to dielectric losses. Furthermore, SEM observations reveal that Co nanoparticles are distributed within the interlayer spaces of the MoS_2 nanosheets, creating abundant heterogeneous interfaces.

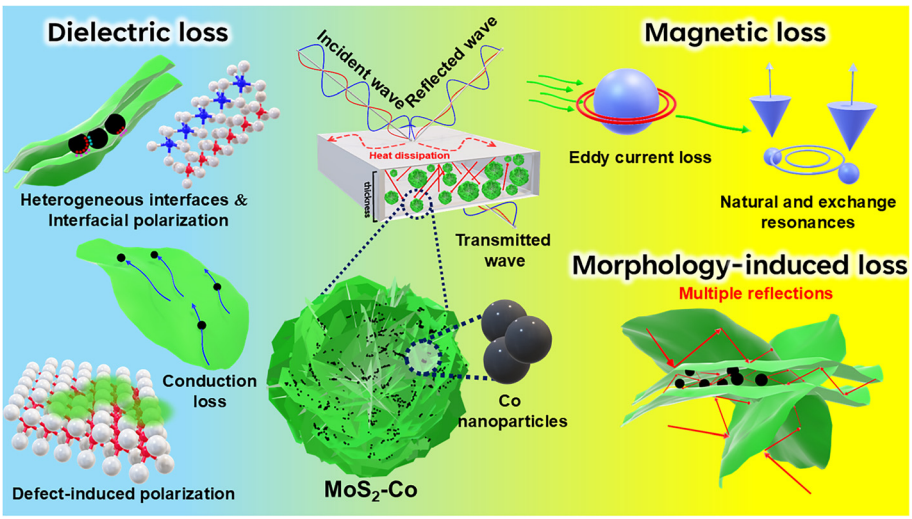

Fig. 16 Possible loss mechanisms contributing the enhanced microwave absorption performance of the synthesized absorbers.

These interfaces act as polarization centers that facilitate charge accumulation and relaxation under alternating EM fields, thereby enhancing interfacial polarization losses. In parallel, the Cole–Cole analyses provide complementary evidence for these dielectric processes. The multiple semicircular arcs in the Cole–Cole plots indicate the coexistence of several relaxation processes, while the tail-like extensions suggest the presence of conductive losses, which may originate from the improved electrical conductivity induced by Co incorporation.

From the magnetic perspective, Co nanoparticles contribute to the absorption through natural and exchange resonances, and eddy current losses, as supported by the permeability and eddy current loss plots. Another key factor influencing absorption efficiency is impedance matching. The synergistic combination of dielectric MoS_2 and magnetic Co nanoparticles provides a magneto–dielectric coupling effect that is beneficial for microwave absorption. The dielectric component contributes mainly through dipolar polarization, defect-induced polarization, interfacial polarization, and conductive loss, while the magnetic Co nanoparticles introduce magnetic loss mechanisms such as natural and exchange resonances. The coexistence of these dielectric and magnetic loss processes enables a better balance between impedance matching and attenuation capability. As a result, the impedance mismatch between free space and the absorber is reduced, allowing incident EMWs to effectively penetrate the material rather than being reflected at the surface, thereby promoting internal energy dissipation. In addition, the hierarchical composite structure promotes multiple internal reflections and scattering of EMWs, which further increases the effective propagation path and enhances energy attenuation. Therefore, the overall microwave absorption performance originates from the cooperative interplay of multiple mechanisms, including defect-induced and interfacial polarization, conductive loss, magnetic resonance processes, optimized impedance matching, and multiple scattering effects, as illustrated in Fig. 16. Such magneto–dielectric synergistic effects ultimately lead to broadband and efficient EMW attenuation in the GHz frequency range.

To reveal the potential of the samples synthesized in this work, the obtained results are compared with those reported

Table 3 Microwave absorption characteristics of the synthesized samples along with the literature data

Materials	Thickness (mm)	RL_{min} (dB)	Frequency (GHz)	EBA (@−10 dB)	Ref.
MoS_2 nanosheets	2.20	−47.80	12.8	4.50	7
Hydrangea-like MoS_2	1.40	−44.67	13.0	3.32	5
Dendritic Co	1.30	—	—	6.00	65
Flower-like Co	2.50	−40.25	6.0	—	66
Co particles	5.00	−19.06	17.4	1.85	67
Fe–MoS_2	2.00	−37.02	—	4.73	9
MoS_2/Ni	2.20	−44.70	9.4	2.40	68
MoS_2/Ni	1.50	—	—	4.00	69
$Ti_3C_2T_x$/polyimide aerogel	3.00	−35.07	—	9.41	70
Sn@C whiskers	2.2	—	—	7.40	71
FeCoNi/bamboo-like carbon fibers	1.80	—	—	5.40	72
Co NPs	4.00	−14.60	10.31	5.36	This work
MoS_2–Co (MC1)	2.00	−15.19	16.51	4.15	
MoS_2–Co (MC3)	3.00	−17.17	13.84	7.51	

in the literature and summarized in Table 3. In addition to MoS_2- and Co-based systems, several recently reported advanced microwave absorber materials, including MXene-based absorbers, carbon-based composites, and magnetic alloy systems, were also incorporated into the comparison table to provide a broader perspective. As shown in the table, the synthesized Co NPs exhibit notably higher or comparable EAB values relative to previously reported Co particles and dendritic Co structures. More importantly, the synthesized MoS_2–Co nanocomposites demonstrate competitive microwave absorption performance compared with many reported Fe- and Ni-based systems as well as several advanced absorber platforms. Considering the simplicity of the synthesis procedure, the absence of complex post-treatments, the short preparation time, and the strong absorption performance achieved, the MoS_2–Co system presents a promising alternative among 2D material–magnetic hybrid absorbers. Notably, even at a relatively low filler loading of 30 wt% in the epoxy matrix, two of the composites exhibited remarkable RL and EAB values, highlighting the high efficiency of the MoS_2–Co combination. These results suggest that the developed composites hold considerable potential for practical applications in microwave absorption, stealth coatings, and electromagnetic interference shielding.

4. Conclusions

In this study, a series of MoS_2–Co nanocomposites with varying Co contents (5–20 wt%) were successfully synthesized, and their microwave absorption performances were systematically evaluated over the 2–18 GHz frequency range. The integration of magnetic Co NPs into the MoS_2 host led to a remarkable enhancement in microwave attenuation performance, primarily due to the synergistic interplay between dielectric and magnetic loss mechanisms. Structural, morphological, compositional, and magnetic characterization studies collectively confirmed the successful incorporation and uniform dispersion of Co within the MoS_2 framework. Among all samples, the MC3 composite (15 wt% Co) exhibited the most superior performance, achieving an RL_{min} of −17.17 dB at 13.84 GHz and an EAB of 7.51 GHz at a thickness of only 3 mm. This outstanding performance is primarily attributed to the optimized balance among dielectric, magnetic, and structural contributions, including defect-induced and interfacial polarization, conductive loss, magnetic resonance processes, optimized impedance matching, and multiple scattering effects, all of which are enhanced by the tailored microstructure and composition. Furthermore, the synergistic magneto–dielectric coupling between MoS_2 and Co nanoparticles contributes to improved impedance matching and enhanced attenuation capability, which together promote efficient microwave absorption. Overall, the MoS_2–Co system, particularly in its MC3 configuration, offers strong potential for advanced stealth applications and other technologies requiring light weight and high-efficiency microwave absorber materials.

Author contributions

B. K.: data curation, formal analysis, investigation, methodology, software, writing – original draft, and writing – review and editing. H. A.: data curation, formal analysis, investigation, methodology, software, resources, supervision, and writing – review and editing. O. A.: data curation and formal analysis. M. K.: data curation and formal analysis. M. A.: conceptualization, data curation, formal analysis, investigation, methodology, project administration, resources, supervision, funding acquisition, and writing – review and editing.

Conflicts of interest

Mustafa Akyol reports that financial support was provided by the Scientific and Technological Research Council of Türkiye.

Data availability

The data that support the findings of this study are available on request from the corresponding author.

Acknowledgements

This study was produced from the PhD thesis of Burak Kıvrak. This work was supported by the Scientific and Technological Research Council of Türkiye (TÜBİTAK) under Grant Number 121F367. The authors thank TÜBİTAK for the financial support.

Declaration of generative AI and AI-assisted technologies in the writing process: During the preparation of this work, the authors used ChatGPT 3.0 in order to correct the grammatical faults in the manuscript. After using this tool/service, the authors reviewed and edited the content as needed and take full responsibility for the content of the published article.

References

1 P. Yin, L. Zhang, X. Feng, J. Wang, J. Dai and Y. Tang, Recent Progress in Ferrite Microwave Absorbing Composites, *Integr. Ferroelectr.*, 2020, **211**(1), 82–101.
2 S. Sharma, S. R. Parne, S. S. S. Panda and S. Gandi, Progress in microwave absorbing materials: A critical review, *Adv. Colloid Interface Sci.*, 2024, **327**, 103143.
3 A. Kumar and S. Singh, Development of Coatings for Radar Absorbing Materials at X-band, IOP Conference Series: Materials Science and Engineering, 2018, vol. 330, p. 012006.
4 J. Li, X. Li, L. He, H. Guo, W. Xia, B. Sun, C. Cao, L. Sha and D. Zhou, MoS_2-Based Nanocomposites for Microwave Absorption: A Review, *ACS Appl. Nano Mater.*, 2024, **7**(6), 5761–5775.

5 W. Zhang, X. Zhang, H. Wu, H. Yan and S. Qi, Impact of morphology and dielectric property on the microwave absorbing performance of MoS_2-based materials, *J. Alloys Compd.*, 2018, **751**, 34–42.
6 M.-Q. Ning, M.-M. Lu, J.-B. Li, Z. Chen, Y.-K. Dou, C.-Z. Wang, F. Rehman, M.-S. Cao and H.-B. Jin, Two-dimensional nanosheets of MoS_2: a promising material with high dielectric properties and microwave absorption performance, *Nanoscale*, 2015, **7**(38), 15734–15740.
7 X. Liang, X. Zhang, W. Liu, D. Tang, B. Zhang and G. Ji, A simple hydrothermal process to grow MoS_2 nanosheets with excellent dielectric loss and microwave absorption performance, *J. Mater. Chem. C*, 2016, **4**(28), 6816–6821.
8 M. F. Elmahaishi, R. a. S. Azis, I. Ismail and F. D. Muhammad, A review on electromagnetic microwave absorption properties: their materials and performance, *J. Mater. Res. Technol.*, 2022, **20**, 2188–2220.
9 J. Pan, X. Sun, T. Wang, Z. Zhu, Y. He, W. Xia and J. He, Porous coin-like Fe@MoS_2 composite with optimized impedance matching for efficient microwave absorption, *Appl. Surf. Sci.*, 2018, **457**, 271–279.
10 H. Wei, Z. Zhang, G. Hussain, L. Zhou, Q. Li and K. Ostrikov, Techniques to enhance magnetic permeability in microwave absorbing materials, *Appl. Mater. Today*, 2020, **19**, 100596.
11 L. L. Adebayo, H. Soleimani, N. Yahya, Z. Abbas, F. A. Wahaab, R. T. Ayinla and H. Ali, Recent advances in the development OF Fe_3O_4-Based microwave absorbing materials, *Ceram. Int.*, 2020, **46**(2), 1249–1268.
12 R. C. Che, C. Y. Zhi, C. Y. Liang and X. G. Zhou, Fabrication and microwave absorption of carbon nanotubes/$CoFe_2O_4$ spinel nanocomposite, *Appl. Phys. Lett.*, 2006, **88**(3), 033105.
13 Y. Wang, X. Gao, X. Wu, W. Zhang, C. Luo and P. Liu, Facile design of 3D hierarchical $NiFe_2O_4$/N-GN/ZnO composite as a high performance electromagnetic wave absorber, *J. Chem. Eng.*, 2019, **375**, 121942.
14 X. Su, J. Wang, X. Zhang, S. Huo, W. Chen, W. Dai and B. Zhang, Design of controlled-morphology $NiCo_2O_4$ with tunable and excellent microwave absorption performance, *Ceram. Int.*, 2020, **46**(6), 7833–7841.
15 M. Zhang, C. Qian, R. Zhu, Z. Jin, Y. Zhang, B. Yang and W. Zhang, Ni-doped Co_3O_4 with micro-nano porous structure as a highly efficient microwave absorber, *J. Alloys Compd.*, 2024, **987**, 174176.
16 Y. Yuan, S. Wei, Y. Liang, B. Wang and Y. Wang, Effect of Solvothermal Reaction-Time on Microstructure and Microwave Absorption Properties of Cobalt Ferrite, *Materials*, 2020, **13**(23), 5331.
17 B. Kıvrak, H. Akyıldız, O. Akgöl, M. Karaaslan and M. Akyol, Polyaniline-Functionalized Nanosized Cobalt Ferrite-Decorated MoS_2 Composites for Broadband Electromagnetic Wave Absorption, *ACS Appl. Electron. Mater.*, 2024, **6**(11), 8211–8225.
18 A. Mondal, A. Mondal, B. Adhikary and D. K. Mukherjee, Cobalt nanoparticles as reusable catalysts for reduction of 4-nitrophenol under mild conditions, *Bull. Mater. Sci.*, 2017, **40**(2), 321–328.
19 S. H. Wu and D. H. Chen, Synthesis and characterization of nickel nanoparticles by hydrazine reduction in ethylene glycol, *J. Colloid Interface Sci.*, 2003, **259**(2), 282–286.
20 V. A. de la Peña O'Shea, P. R. de la Piscina, N. Homs, G. Aromí and J. L. G. Fierro, Development of Hexagonal Closed-Packed Cobalt Nanoparticles Stable at High Temperature, *Chem. Mater.*, 2009, **21**(23), 5637–5643.
21 A. F. Khusnuriyalova, M. Caporali, E. Hey-Hawkins, O. G. Sinyashin and D. G. Yakhvarov, Preparation of Cobalt Nanoparticles, *Eur. J. Inorg. Chem.*, 2021, **2021**(30), 3023–3047.
22 F. Guo, H. Zheng, Z. Yang and Y. Qian, Synthesis of cobalt nanoparticles in ethanol hydrazine alkaline system (EHAS) at room temperature, *Mater. Lett.*, 2002, **56**(6), 906–909.
23 V. F. Puntes, K. Krishnan and A. P. Alivisatos, Synthesis of Colloidal Cobalt Nanoparticles with Controlled Size and Shapes, *Top. Catal.*, 2002, **19**(2), 145–148.
24 D. P. Dinega and M. G. Bawendi, A Solution-Phase Chemical Approach to a New Crystal Structure of Cobalt, *Angew. Chem., Int. Ed.*, 1999, **38**(12), 1788–1791.
25 H. K. Choudhary, M. Manjunatha, R. Damle, K. P. Ramesh and B. Sahoo, Solvent dependent morphology and ^{59}Co internal field NMR study of Co-aggregates synthesized by a wet chemical method, *Phys. Chem. Chem. Phys.*, 2018, **20**(26), 17739–17750.
26 R. Kumar, M. Manjunatha, A. V. Anupama, K. P. Ramesh and B. Sahoo, Synthesis, composition and spin-dynamics of FCC and HCP phases of pyrolysis derived Co-nanoparticles embedded in amorphous carbon matrix, *Ceram. Int.*, 2019, **45**(16), 19879–19887.
27 T. Prabhakaran, R. V. Mangalaraja, J. C. Denardin and K. Varaprasad, The effect of capping agents on the structural and magnetic properties of cobalt ferrite nanoparticles, *J. Mater. Sci.: Mater. Electron.*, 2018, **29**(14), 11774–11782.
28 S. Yougbaré, C. Mutalik, P.-F. Chung, D. I. Krisnawati, F. Rinawati, H. Irawan, H. Kristanto and T.-R. Kuo, Gold Nanorod-Decorated Metallic MoS_2 Nanosheets for Synergistic Photothermal and Photodynamic Antibacterial Therapy, *Nanomaterials*, 2021, **11**(11), 3064.
29 S. V. P. Vattikuti and C. Byon, Synthesis and Characterization of Molybdenum Disulfide Nanoflowers and Nanosheets: Nanotribology, *J. Nanomater.*, 2015, **2015**, 710462.
30 K. M. Cole, D. W. Kirk and S. J. Thorpe, Co_3O_4 nanoparticles characterized by XPS and UPS, *Surf. Sci. Spectra*, 2021, **28**(1), 014001.
31 E. Er and N. Erk, Construction of a sensitive electrochemical sensor based on 1T-MoS_2 nanosheets decorated with shape-controlled gold nanostructures for the voltammetric determination of doxorubicin, *Microchim. Acta*, 2020, **187**(4), 223.
32 M. Rajput, S. K. Mallik, S. Chatterjee, A. Shukla, S. Hwang, S. Sahoo, G. V. P. Kumar and A. Rahman, Defect-engin-

eered monolayer MoS_2 with enhanced memristive and synaptic functionality for neuromorphic computing, *Commun. Mater.*, 2024, **5**(1), 190.

33 M. Wang, H. Yang, K. Shen, H. Xu, W. Wang, Z. Yang, L. Zhang, J. Chen, Y. Huang, M. Chen, D. Mitlin and X. Li, Stable Lithium Sulfur Battery Based on In Situ Electrocatalytically Formed Li_2S on Metallic MoS_2−Carbon Cloth Support, *Small Methods*, 2020, **4**(9), 2000353.

34 Y. Bi, M. Ma, Y. Liu, Z. Tong, R. Wang, K. L. Chung, A. Ma, G. Wu, Y. Ma, C. He, P. Liu and L. Hu, Microwave absorption enhancement of 2-dimensional CoZn/C@MoS_2@PPy composites derived from metal-organic framework, *J. Colloid Interface Sci.*, 2021, **600**, 209–218.

35 C. Wang, X. Han, X. Zhang, S. Hu, T. Zhang, J. Wang, Y. Du, X. Wang and P. Xu, Controlled Synthesis and Morphology-Dependent Electromagnetic Properties of Hierarchical Cobalt Assemblies, *J. Phys. Chem. C*, 2010, **114**(35), 14826–14830.

36 B. Quan, X. Liang, G. Xu, Y. Cheng, Y. Zhang, W. Liu, G. Ji and Y. Du, A permittivity regulating strategy to achieve high-performance electromagnetic wave absorbers with compatibility of impedance matching and energy conservation, *New J. Chem.*, 2017, **41**(3), 1259–1266.

37 J. Xu, Y. Yang, H. Dong, J. Li, Y. Ma, M. Wang, C. Zhu, X. Zhang, G. Zheng, W. Ding and Z. Sheng, The effect of conduction loss on microwave absorption performance of Fe-doped $NiCo_2O_4$ spinel oxide, *Ceram. Int.*, 2024, **50**(22, Part B), 46882–46891.

38 Y. Liu, Y. Zhang, X. Wang, Z. Wang, W. Lai, X. Zhang and X. Liu, Excellent Microwave Absorbing Property of Multiwalled Carbon Nanotubes with Skin–Core Heterostructure Formed by Outer Dominated Fluorination, *J. Phys. Chem. C*, 2018, **122**(11), 6357–6367.

39 M. Ling, J. Wu, P. Liu, F. Wu, L. Zhang, M. R. Tariq and B. Zhang, Three-dimensional n-$MoSe_2$/GOx (n= 1T, 1T' and 2H) microsphere: Phase-modulation strategy and microwave absorbing mechanism, *Carbon*, 2024, **230**, 119614.

40 L. Guo, Q. An, Z.-Y. Xiao, S.-R. Zhai, W. Cai, H. Wang and Z. Li, Constructing Stacked Structure of S-Doped Carbon Layer-Encapsulated MoO_2 NPs with Dominated Dielectric Loss for Microwave Absorption, *ACS Sustainable Chem. Eng.*, 2019, **7**(24), 19546–19555.

41 S. Zheng, L. Lyu, F. Wang, Y. Liu and J. Liu, Self-supported construction of three-dimensional $NiCo_2O_4$ hierarchical nanoneedles for high-performance microwave absorption, *Ceram. Int.*, 2021, **47**(24), 34289–34296.

42 S. Wang, H. Zhang, Q. Liu and X. Kong, Magnetic carbon nanotubes-based microwave absorbents: Review and perspective, *Synth. Methods*, 2022, **291**, 117198.

43 M. Cao, X. Wang, W. Cao, X. Fang, B. Wen and J. Yuan, Thermally Driven Transport and Relaxation Switching Self-Powered Electromagnetic Energy Conversion, *Small*, 2018, **14**(29), 1800987.

44 Z. Feng, C. Liu, X. Li, G. Luo, N. Zhai, R. Hu, J. Lin, J. Peng, Y. Peng and R. Che, Designing Electronic Structures of Multiscale Helical Converters for Tailored Ultrabroad Electromagnetic Absorption, *Nano-Micro Lett.*, 2024, **17**(1), 20.

45 H. Wei, S. Chen, Z. Chen, L. Tang, J. Xue, C. Wang, Z. Wang and Y. Li, Hetero–interface engineering of biomass carbon foam for broadband microwave absorption and thermal insulation properties, *Carbon*, 2025, **241**, 120385.

46 Y. Wu, R. Shu, X. Shan, J. Zhang, J. Shi, Y. Liu and M. Zheng, Facile design of cubic-like cerium oxide nanoparticles decorated reduced graphene oxide with enhanced microwave absorption properties, *J. Alloys Compd.*, 2020, **817**, 152766.

47 X. Cui, W. Liu, W. Gu, X. Liang and G. Ji, Two-dimensional MoS_2 modified using $CoFe_2O_4$ nanoparticles with enhanced microwave response in the X and Ku band, *Inorg. Chem. Front.*, 2019, **6**(2), 590–597.

48 D. Chen, G.-S. Wang, S. He, J. Liu, L. Guo and M.-S. Cao, Controllable fabrication of mono-dispersed RGO–hematite nanocomposites and their enhanced wave absorption properties, *J. Mater. Chem. A*, 2013, **1**(19), 5996–6003.

49 X. G. Liu, Z. Q. Ou, D. Y. Geng, Z. Han, J. J. Jiang, W. Liu and Z. D. Zhang, Influence of a graphite shell on the thermal and electromagnetic characteristics of FeNi nanoparticles, *Carbon*, 2010, **48**(3), 891–897.

50 M. Qin, D. Lan, G. Wu, X. Qiao and H. Wu, Sodium citrate assisted hydrothermal synthesis of nickel cobaltate absorbers with tunable morphology and complex dielectric parameters toward efficient electromagnetic wave absorption, *Appl. Surf. Sci.*, 2020, **504**, 144480.

51 M. Qin, L. Zhang and H. Wu, Dielectric Loss Mechanism in Electromagnetic Wave Absorbing Materials, *Adv. Sci.*, 2022, **9**(10), 2105553.

52 F. Hu, P. Zhang, P. Ding, S. Zhang, B. Fan, A. S. Shamshirgar, W. Zheng, W. Sun, L. Cai, H. Xie, Q. Shao, J. Rosen and Z. Sun, Magnetic–Dielectric Synergy in One-Dimensional Metal Heterostructures for Enhanced Low-Frequency Microwave Absorption, *Nano-Micro Lett.*, 2026, **18**(1), 155.

53 L. Deng and M. Han, Microwave absorbing performances of multiwalled carbon nanotube composites with negative permeability, *Appl. Phys. Lett.*, 2007, **91**(2), 023119.

54 X. Xiang, Z. Yang, G. Fang, Y. Tang, Y. Li, Y. Zhang, D.-H. Kim and C. Liu, Tailoring tactics for optimizing microwave absorbing behaviors in ferrite materials, *Mater. Today Phys.*, 2023, **36**, 101184.

55 Y. Zhang, X. Wang and M. Cao, Confinedly implanted $NiFe_2O_4$-rGO: Cluster tailoring and highly tunable electromagnetic properties for selective-frequency microwave absorption, *Nano Res.*, 2018, **11**(3), 1426–1436.

56 F. Wen, H. Yi, L. Qiao, H. Zheng, D. Zhou and F. Li, Analyses on double resonance behavior in microwave magnetic permeability of multiwalled carbon nanotube composites containing Ni catalyst, *Appl. Phys. Lett.*, 2008, **92**(4), 042507.

57 W. Ma, X. Liu, T. Yang, J. Wang, Z. Qiu, Z. Cai, P. Bai, X. Ji and Y. Huang, Strong Magnetic–Dielectric Synergistic

Gradient Metamaterials for Boosting Superior Multispectral Ultra-Broadband Absorption with Low-Frequency Compatibility, *Adv. Funct. Mater.*, 2025, **35**(18), 2314046.

58 Y. Wei, K. Zhong, T. Jiang, J. Zhang, K. Bi, L. Li and Y. Peng, Gumdrop-cake-like CuNi/C nanofibers with tunable microstructure for microwave absorbing application, *Ceram. Int.*, 2020, **46**(8, Part A), 11406–11415.

59 J. Gao, Z. Ma, F. Liu and C. Chen, Synthesis of carbon-coated cobalt ferrite core–shell structure composite: A method for enhancing electromagnetic wave absorption properties by adjusting impedance matching, *Chin. J. Chem. Eng.*, 2022, **47**, 206–217.

60 J. Liu, Z. Jia, W. Zhou, X. Liu, C. Zhang, B. Xu and G. Wu, Self-assembled MoS_2/magnetic ferrite $CuFe_2O_4$ nanocomposite for high-efficiency microwave absorption, *J. Chem. Eng.*, 2022, **429**, 132253.

61 B. Kıvrak, PhD Thesis, Konya Technical University, 2025.

62 Y. Hou, Z. Sheng, C. Fu, J. Kong and X. Zhang, Hygroscopic holey graphene aerogel fibers enable highly efficient moisture capture, heat allocation and microwave absorption, *Nat. Commun.*, 2022, **13**(1), 1227.

63 K. Bi, Y. Guo, J. Zhou, G. Dong, H. Zhao, Q. Zhao, Z. Xiao, X. Liu and C. Lan, Negative and near zero refraction metamaterials based on permanent magnetic ferrites, *Sci. Rep.*, 2014, **4**(1), 4139.

64 H. Yuan, Z. Liu, Y. Zhang, J. Ding, Y. Sun, M. Zhang and S. Tan, High-performance electromagnetic wave absorption in cobalt sulfide flower-like nanospheres, *RSC Adv.*, 2022, **12**(39), 25323–25331.

65 K. Tian, Q. Zhang, X. Liu, C. Zhang and F. Yang, Synthesis of dendritic cobalt with flower-like structure by a facile wet chemistry method as an excellent electromagnetic wave absorber, *J. Colloid Interface Sci.*, 2023, **649**, 58–67.

66 G. Tong, J. Yuan, W. Wu, Q. Hu, H. Qian, L. Li and J. Shen, Flower-like Co superstructures: Morphology and phase evolution mechanism and novel microwave electromagnetic characteristics, *CrystEngComm*, 2012, **14**(6), 2071–2079.

67 S. Wen, Y. Liu, X. Zhao, J. Cheng and H. Li, Facile synthesis of novel cobalt particles by reduction method and their microwave absorption properties, *Powder Technol.*, 2014, **264**, 128–132.

68 Y. Liu, C. Ji, X. Su, X. He, J. Xu and Y. Li, Enhanced microwave absorption properties of flaky MoS_2 powders by decorating with Ni particles, *J. Magn. Magn. Mater.*, 2020, **511**, 166961.

69 Z. Zhang, Z. Wang, L. Heng, S. Wang, X. Chen, X. Fu, Y. Zou and Z. Tang, Improving the Electromagnetic Wave Absorption Properties of the Layered MoS_2 by Cladding with Ni Nanoparticles, *J. Phys. Soc. Jpn.*, 2018, **87**(5), 054402.

70 X. Wang, X. Chen, Q. He, Y. Hui, C. Xu, B. Wang, F. Shan, J. Zhang and J. Shao, Bidirectional, Multilayer MXene/Polyimide Aerogels for Ultra-Broadband Microwave Absorption, *Adv. Mater.*, 2024, **36**(36), 2401733.

71 F. Hu, P. Ding, F. Wu, P. Zhang, W. Zheng, W. Sun, R. Zhang, L. Cai, B. Fan and Z. Sun, Novel cable-like tin@-carbon whiskers derived from the Ti_2SnC MAX phase for ultra-wideband electromagnetic wave absorption, *Carbon Energy*, 2024, **6**(12), e638.

72 X. Yang, B. Qiu, X. Li, X. Liu and X. Fan, *In situ* growth of FeCoNi nanoparticles onto 1D bamboo fiber carbon for enhanced electromagnetic wave absorption, *Carbon*, 2024, **219**, 118804.